



HAL
open science

Discovery of Magnetospheric Interactions in the Doubly-Magnetic Hot Binary ϵ Lupi

Ayan Biswas, Barnali Das, Poonam Chandra, Gregg A Wade, Matthew E Shultz, Francesco Cavallaro, Veronique Petit, Patrick A Woudt, Evelyne Alecian

► **To cite this version:**

Ayan Biswas, Barnali Das, Poonam Chandra, Gregg A Wade, Matthew E Shultz, et al.. Discovery of Magnetospheric Interactions in the Doubly-Magnetic Hot Binary ϵ Lupi. Monthly Notices of the Royal Astronomical Society, 2023, 523 (4), pp.5155-5170. 10.1093/mnras/stad1756 . hal-04150085

HAL Id: hal-04150085

<https://hal.science/hal-04150085>

Submitted on 24 May 2024

HAL is a multi-disciplinary open access archive for the deposit and dissemination of scientific research documents, whether they are published or not. The documents may come from teaching and research institutions in France or abroad, or from public or private research centers.

L'archive ouverte pluridisciplinaire **HAL**, est destinée au dépôt et à la diffusion de documents scientifiques de niveau recherche, publiés ou non, émanant des établissements d'enseignement et de recherche français ou étrangers, des laboratoires publics ou privés.

Discovery of magnetospheric interactions in the doubly magnetic hot binary ϵ Lupi

Ayan Biswas^{1,2,3*}, Barnali Das^{1,4}, Poonam Chandra^{1,5,1}, Gregg A. Wade³, Matthew E. Shultz⁴,
 Francesco Cavallaro^{1,6}, Veronique Petit^{1,4}, Patrick A. Woudt^{1,6} and Evelyne Alecian⁷

¹National Centre for Radio Astrophysics, Tata Institute of Fundamental Research, Ganeshkhind, Pune-411007, India

²Department of Physics, Engineering Physics & Astronomy, Queen's University, Kingston, Ontario K7L 3N6, Canada

³Department of Physics & Space Science, Royal Military College of Canada, PO Box 17000 Station Forces, Kingston, ON K7K 0C6, Canada

⁴Department of Physics and Astronomy, University of Delaware, Newark, DE 19716, USA

⁵National Radio Astronomy Observatory, 520 Edgemont Road, Charlottesville VA 22903, USA

⁶Inter-University Institute for Data Intensive Astronomy, Department of Astronomy, University of Cape Town, Private Bag X3, Rondebosch 7701, South Africa

⁷Univ. Grenoble Alpes, CNRS, IPAG, F-38000 Grenoble, France

Accepted 2023 June 8. Received 2023 June 8; in original form 2023 January 1

ABSTRACT

Magnetic fields are extremely rare in close, hot binaries, with only 1.5 per cent of such systems known to contain a magnetic star. The eccentric ϵ Lupi system stands out in this population as the only close binary in which both stars are known to be magnetic. We report the discovery of strong variable radio emission from ϵ Lupi using the upgraded Giant Metrewave Radio Telescope (uGMRT) and the MeerKAT radio telescope. The light curve exhibits striking unique characteristics including sharp high-amplitude pulses that repeat with the orbital period, with the brightest enhancement occurring near periastron. The characteristics of the light curve point to variable levels of magnetic reconnection throughout the orbital cycle, making ϵ Lupi the first known high-mass, main sequence binary embedded in an interacting magnetosphere. We also present a previously unreported enhancement in the X-ray light curve obtained from archival *XMM-Newton* data. The stability of the components' fossil magnetic fields, the firm characterization of their relatively simple configurations, and the short orbital period of the system make ϵ Lupi an ideal target to study the physics of magnetospheric interactions. This system may thus help us to illuminate the exotic plasma physics of other magnetically interacting systems such as moon–planet, planet–star, and star–star systems including T Tauri binaries, RS CVn systems, and neutron star binaries.

Key words: radiation mechanisms: non-thermal – binaries: close – stars: individual: (HD136504) – stars: magnetic field – stars: massive – stars: variables: general.

1 INTRODUCTION

A small fraction of hot massive stars have been found to harbour extremely stable, ordered (usually dipolar) magnetic fields, which are of \sim kG strength (Wade et al. 2014; Grunhut et al. 2017). The presence of such organized surface magnetic fields can channel and confine the outflowing stellar winds (Babel & Montmerle 1997), creating a magnetosphere that can radiate in various wavebands (Andre et al. 1988; Linsky, Drake & Bastian 1992). The confinement of the wind in the magnetosphere leads to the suppression of mass-loss (ud-Doula & Owocki 2002; Petit et al. 2017). The magnetic field thus plays a crucial role in deciding the mass of the magnetic star at the end of the main sequence (Keszthelyi et al. 2019, 2020). Petit et al. (2017) have shown that magnetospheric mass-loss suppression is a possible formation channel for the production of the heavy stellar-mass black holes such as those detected by gravitational wave observatories (Abbott et al. 2016a, b).

Binarity impacts stellar populations in numerous ways, such as by modifying surface abundances, enriching the interstellar medium, and affecting the demise of massive stars as supernova and γ -ray burst explosions (Izzard et al. 2006). In the Binarity and Magnetic Interactions in various classes of Stars (BinaMIcS) survey, about 170 short-period double-lined spectroscopic intermediate-mass and high-mass binaries with orbital periods of less than 20 d were observed with high-resolution spectropolarimeters, of which only 1.5 per cent were found to contain a magnetic star (Alejian et al. 2015). This fraction is much lower than the percentage of isolated intermediate-mass and high-mass magnetic stars (\sim 10 per cent; Grunhut et al. 2017; Sikora et al. 2019). Among the magnetic binaries of this survey, magnetic fields have been detected in only one of the two components, with the sole exception of ϵ Lupi A (henceforth, referred to as ϵ Lupi). Shultz et al. (2015) reported dipolar surface magnetic field strengths (B_d) of roughly 0.8 and 0.5 kG in the primary and secondary components of ϵ Lupi, respectively.

Apart from ϵ Lupi, there exist just two other reported doubly magnetic hot binary systems, HD 156424 (Shultz et al. 2021) and BD+40 175 (El'kin 1999; Semenko, Kichigina & Kuchaeva

* E-mail: ayan.scc2@gmail.com, ayan.biswas@queensu.ca

Table 1. Different stellar and orbital parameters of ϵ Lupi. Parameters with subscript ‘phot’ represent parameters obtained from photometric observations by Pablo et al. (2019), whereas parameters with subscript ‘spec’ represent parameters obtained from spectroscopic observations by Shultz et al. (2019).

Parameters	Primary	Secondary
<i>Stellar parameters</i>		
Mass ($M_{\text{phot}}/M_{\odot}$) ^a	11.0 ^{2.9} _{-2.2}	9.2 ^{2.4} _{-1.9}
Mass ($M_{\text{spec}}/M_{\odot}$) ^b	7.7 ± 0.5	6.4 ± 0.3
Radius ($R_{\text{phot}}/R_{\odot}$) ^a	4.64 ^{0.37} _{-0.48}	4.83 ^{0.42} _{-0.46}
Radius ($R_{\text{spec}}/R_{\odot}$) ^b	5.1 ± 0.07	3.7 ± 0.5
Luminosity (L/L_{\odot}) ^a	3407 ⁶⁵⁸ ₋₅₆₇	2197 ⁴⁸⁹ ₋₃₉₉
Effective temperature, T_{eff} (K) ^a	20 500	18 000
$v \sin i$ (kms ⁻¹) ^d	35 ± 10	35 ± 5
Obliquity, β (°) ^a	<30.7	<21.4
Dipolar field strength, B_p (kG) ^a	>0.79	>0.5
$\log(R_A/R_K)$ ^a	0.63 ± 0.07	0.22 ± 0.08
<i>Orbital parameters</i>		
Orbital period, P_{orb} (days) ^a	4.559 646 ^{0.000005} _{-0.000008}	
T_0 (HJD – 2400 000) ^a	2439 379.875 ^{0.024} _{-0.019}	
Eccentricity (e) ^a	0.2806 ^{0.0059} _{-0.0047}	
Semi-major axis, a (R_{\odot}) ^a	31.5 ^{2.5} _{-2.3}	
Apsidal motion $\frac{d\omega}{dt}$ (°/yr) ^a	1.1 ^{0.1} _{-0.1}	

Notes. ^aPablo et al. (2019) ^bShultz et al. (2019) ^cShultz et al. (2015) ^dShultz et al. (2018b).

2011). Both systems have long (years to decades) orbital periods, implying that their stellar components evolve practically as single stars. In contrast, the short orbital period ($P_{\text{orb}} \sim 4.6$ d) of ϵ Lupi implies the possibility of significant tidal interactions and potentially magnetospheric interactions as well (Pablo et al. 2019).

In recent years, extensive studies have been performed of magnetism in intermediate-mass and high-mass stars, aiming at characterizing various magnetospheric emissions such as H α , X-ray, UV, IR, and non-thermal radio emission (Nazé et al. 2014; Oksala et al. 2015; Shultz et al. 2020; Erba et al. 2021; Leto et al. 2021; Das, Chandra & Petit 2022a; Das et al. 2022c). These studies together have been able to provide a plethora of information regarding the three-dimensional structure of their magnetospheres (Townsend & Owocki 2005; ud-Doula et al. 2013; Leto et al. 2016; Das & Chandra 2021). The effect of binarity in the evolution of massive stars has been studied in great detail (e.g. Sana et al. 2012). But the study of the combined effects of binarity and magnetic fields on massive star magnetospheres is in its infancy (e.g. Shultz et al. 2018b). The doubly magnetic massive binary system ϵ Lupi provides us with a unique test-bed to examine such effects. Studying this system may help understand similar magnetically interacting binaries e.g. moon-planet, planet-star, and star-star systems including T Tauri binaries (Massi et al. 2006; Salter et al. 2010; Tofflemire et al. 2017), RS CVn systems (Uchida & Sakurai 1983; Karmakar et al. 2023), and neutron star binaries (Wang et al. 2018; Cherkis & Lyutikov 2021; Most & Philippov 2022, 2023).

1.1 ϵ Lupi

ϵ Lupi is a double-lined spectroscopic binary (SB2) in a close orbit (Uytterhoeven et al. 2005) where the component spectral types are identified as B3IV and B3V (Moore 1911; Campbell & Moore

1928; Thackeray 1970). Pablo et al. (2019) discovered a ‘heart-beat’ type light curve from photometric observations obtained with the BRiGht-star Target Explorer (BRITE) constellation of space telescopes (Weiss et al. 2014), which they interpreted as a result of tidal distortion. Such light curves are normally observed in systems with high eccentricities, and can be used to determine different orbital parameters, and to directly measure masses and radii. Pablo et al. (2019) determined an eccentric orbit ($e = 0.28$) with an orbital period of approximately 4.6 d. The primary and the secondary possess comparable masses ($M_p = 11.0 M_{\odot}$ & $M_s = 9.2 M_{\odot}$), radii ($R_p = 4.6 R_{\odot}$ & $R_s = 4.8 R_{\odot}$) and effective temperatures ($T_{\text{eff},p} = 20.5$ kK & $T_{\text{eff},s} = 18$ kK) (Table 1). The orbit of ϵ Lupi is characterized very well with the help of numerous radial velocity measurements (Thackeray 1970; Uytterhoeven et al. 2005; Pablo et al. 2019). However, the rotational periods of the two components are not known. The longitudinal magnetic fields (B_z) of the components show weak temporal modulation that points toward the magnetic axes being approximately aligned with the rotational axes (Fig. 3, bottom). The constant positive and negative (B_z) for the secondary and primary, respectively, shows that the field axes are anti-aligned. In such a scenario, where the rotation axes are aligned, magnetic axes are anti-aligned, and the obliquity of the field with respect to the rotation axis in each star is assumed to be small, the energy due to the magnetic dipole–dipole interaction force is at a minimum, making this a stable configuration (Pablo et al. 2019).

To obtain the radio light curve with respect to orbital phase, we used the following ephemeris reported by Pablo et al. (2019):

$$\text{HJD} = T_0 + P_{\text{orb}} E, \quad (1)$$

where E is the phase of the observation, $P_{\text{orb}} = 4.559 646^{0.000005}_{-0.000008}$ is the orbital period, and $T_0 = 2439 379.875^{0.024}_{-0.019}$ is defined by the reference periastron phase. The system has a significant apsidal motion with $d\omega/dt = 1.1 \pm 0.1^\circ \text{ yr}^{-1}$ (Pablo et al. 2019). Orbital phases calculated in this article account for apsidal motion unless stated otherwise.

Shultz et al. (2015) predicted that the magnetospheres of the two stars are always overlapping, and that the strength of the interaction should change over the orbital cycle due to the eccentricity (Table 1). The system was undetected in H α and UV (Petit et al. 2013; Shultz et al. 2019); but it was detected in X-rays with *XMM-Newton* (Nazé et al. 2014, see Section 2.3 for details) and NICER (Das et al. 2023). In this paper, we first time report the radio observations and detection of ϵ Lupi system. Since radio emission is common in magnetic hot stars (Leto et al. 2021; Shultz et al. 2022), radio observations may be the best way to probe its magnetosphere. The magnetospheric interactions that one would expect due to overlapping magnetospheres may be witnessed as enhancements in radio and/or X-ray light curves. In this paper, we report the discovery of radio emission and present a detailed radio study of ϵ Lupi with the upgraded Giant Metrewave Radio Telescope (uGMRT; Swarup 1992; Gupta et al. 2017) and the MeerKAT radio telescope (Jonas 2009). We also perform the first time series analysis of the archival *XMM-Newton* data of 8 ksec observation.

This paper is structured as follows: The observation details and data analysis procedures are explained in Section 2. In Section 3, we present results from the radio observations. In Section 4, we explore a variety of models in order to interpret the results in the context of magnetospheric interaction. Finally, in Section 5, we summarize our conclusions.

Table 2. Observation details and imaging results of uGMRT observations. For each observing day, only mean phases are mentioned for simplicity. The bold faced phases represent periastron observations (defined by phase 0 ± 0.02). As the observations during May 2022 are of short-duration, flux density values for small-duration scans are not shown individually in those cases.

Obs. Date	Mean phase ϕ_{orb}	Heliocentric Julian Date (HJD-2459000)	Band 5		Band 4	
			F ₁₂₅₀ (mJy)	rms ($\mu\text{Jy beam}^{-1}$)	F ₇₅₀ (mJy)	rms ($\mu\text{Jy beam}^{-1}$)
2021 Jan 02	0.340 \pm 0.003	216.64407 \pm 0.01320	2.905 \pm 0.045	16.76	1.828 \pm 0.084	37.87
	0.349 \pm 0.003	216.68194 \pm 0.01320	2.754 \pm 0.049	17.86	1.882 \pm 0.072	38.18
	0.355 \pm 0.002	216.70935 \pm 0.00727	2.872 \pm 0.082	21.09	1.844 \pm 0.093	44.61
2021 Jan 05	0.000 \pm 0.003	219.64982 \pm 0.01320	4.270 \pm 0.110	38.99	2.003 \pm 0.069	38.72
	0.007 \pm 0.003	219.68246 \pm 0.01320	4.520 \pm 0.130	40.98	2.069 \pm 0.076	35.63
	0.014 \pm 0.003	219.71649 \pm 0.01320	4.600 \pm 0.100	36.60	2.058 \pm 0.082	40.13
	0.020 \pm 0.001	219.74288 \pm 0.00556	4.440 \pm 0.110	49.80	2.047 \pm 0.091	45.20
2021 Jan 08	0.651 \pm 0.003	222.61876 \pm 0.01320	2.797 \pm 0.045	21.02	1.630 \pm 0.029	29.21
	0.658 \pm 0.003	222.65279 \pm 0.01320	2.770 \pm 0.077	36.14
	0.666 \pm 0.003	222.68613 \pm 0.01320	2.840 \pm 0.056	24.61
	0.674 \pm 0.004	222.72363 \pm 0.01667	2.500 \pm 0.063	27.18
2021 Jan 15	0.186 \pm 0.003	229.61876 \pm 0.01320	2.230 \pm 0.039	22.51	1.268 \pm 0.072	35.97
	0.193 \pm 0.003	229.65279 \pm 0.01320	2.289 \pm 0.038	21.69	1.272 \pm 0.066	34.07
	0.201 \pm 0.003	229.68613 \pm 0.01320	2.243 \pm 0.040	24.31	1.302 \pm 0.074	35.15
	0.209 \pm 0.001	229.72363 \pm 0.00556	2.185 \pm 0.045	27.93	1.236 \pm 0.077	45.42
2021 Jan 18	0.836 \pm 0.003	232.58476 \pm 0.01320	2.140 \pm 0.053	22.51	1.547 \pm 0.054	32.50
	0.844 \pm 0.003	232.62014 \pm 0.01320	2.125 \pm 0.035	24.44	1.629 \pm 0.042	35.08
	0.851 \pm 0.003	232.65347 \pm 0.01320	2.093 \pm 0.041	25.81	1.426 \pm 0.070	51.29
	0.858 \pm 0.002	232.68264 \pm 0.00903	1.942 \pm 0.040	25.39	1.401 \pm 0.067	54.17
2021 Feb 06	0.010 \pm 0.006	251.49313 \pm 0.02573	1.978 \pm 0.073	34.69
2021 Feb 22	0.491 \pm 0.003	267.48709 \pm 0.01250	2.299 \pm 0.045	24.26	1.414 \pm 0.120	63.02
	0.498 \pm 0.003	267.51973 \pm 0.01250	2.235 \pm 0.059	24.53	1.375 \pm 0.063	37.03
	0.506 \pm 0.003	267.55515 \pm 0.01250	2.088 \pm 0.046	25.38	1.279 \pm 0.072	37.10
	0.513 \pm 0.003	267.58988 \pm 0.01459	2.155 \pm 0.042	26.04	1.168 \pm 0.063	37.19
2021 Jul 20	0.070 \pm 0.002	416.04451 \pm 0.01041	2.899 \pm 0.092	40.67	1.380 \pm 0.100	57.46
	0.076 \pm 0.002	416.07228 \pm 0.01041	2.720 \pm 0.110	38.43	1.630 \pm 0.170	91.58
	0.082 \pm 0.002	416.09589 \pm 0.00694	2.624 \pm 0.099	41.71	1.310 \pm 0.110	63.83
2021 Aug 24	0.743 \pm 0.002	451.02847 \pm 0.01041	3.459 \pm 0.058	29.85	1.790 \pm 0.160	65.87
	0.750 \pm 0.002	451.06308 \pm 0.01041	3.538 \pm 0.062	30.75	1.460 \pm 0.140	70.28
	0.7564 \pm 0.002	451.09155 \pm 0.01041	3.496 \pm 0.069	44.32	0.967 \pm 0.128	80.25
2021 Sep 08	0.010 \pm 0.007	465.96733 \pm 0.03330	4.490 \pm 0.023	24.60
2022 May 20	0.785 \pm 0.005	720.25251 \pm 0.02361	2.439 \pm 0.052	30.71	1.473 \pm 0.088	61.90
2022 May 26	0.097 \pm 0.008	726.22645 \pm 0.03710	4.102 \pm 0.068	31.20
2022 May 29	0.749 \pm 0.005	729.20490 \pm 0.02396	3.685 \pm 0.083	49.95	1.660 \pm 0.160	63.61
2022 May 30	0.965 \pm 0.005	730.19134 \pm 0.02361	3.359 \pm 0.085	37.36

2 OBSERVATIONS AND DATA REDUCTION

2.1 The uGMRT

As binarity may lead to variations in the radio flux density on the time-scale of the orbital period, we sampled various phases across the orbital cycle of ϵ Lupi ($P_{\text{orb}} \sim 4.56$ d) with the uGMRT to check for variability in the radio emission. In addition, to obtain spectra at different phases, we performed simultaneous measurements in band 5 (1050–1450 MHz) and band 4 (550–900 MHz) in a sub-array mode where each array contained roughly 14 antennae distributed along the Y-shaped arms of uGMRT. The sub-array mode was chosen with an intention to avoid the possibility of spurious results regarding spectral properties over band 4 and band 5 due to time-variability (if there is any). Initially, the target was observed at six different orbital phases. The observations were taken between 2021 January 02 and 2021 February 22 (see Table 2) during uGMRT Cycle 39 (ObsID: 39_086, PI: A. Biswas). Three additional observations were taken between

2021 July 20 and 2021 September 08 under Director’s Discretionary Time (DDT) proposal (ObsID: ddtC_189). Finally, four additional follow-up observations are reported here that were taken during 2022 May, under uGMRT Cycle 42 (ObsID: 42_018, PI: A. Biswas). The February 06 and September 08 (2021) observations were not carried out in sub-array mode, and all 30 antennae of uGMRT were used in the band 4 and the band 5 frequency settings, respectively.

Each observation was of approximately 4 h, with an on-source time of 100–150 min. For all observations, visibilities were recorded in full polar mode with a bandwidth of 400 MHz divided into 2048 frequency channels in both frequency bands. The standard flux calibrator J1331+305 (also known as 3C286) was observed at the beginning (and sometimes also towards the end) for 10–15 min to calibrate the absolute flux density scale. Each scan of the target was preceded and followed by a 5-min observation of the phase calibrator J1626–298 chosen from the Very Large Array calibrator list such that it is located within 15° of ϵ Lupi. The phase calibrator was

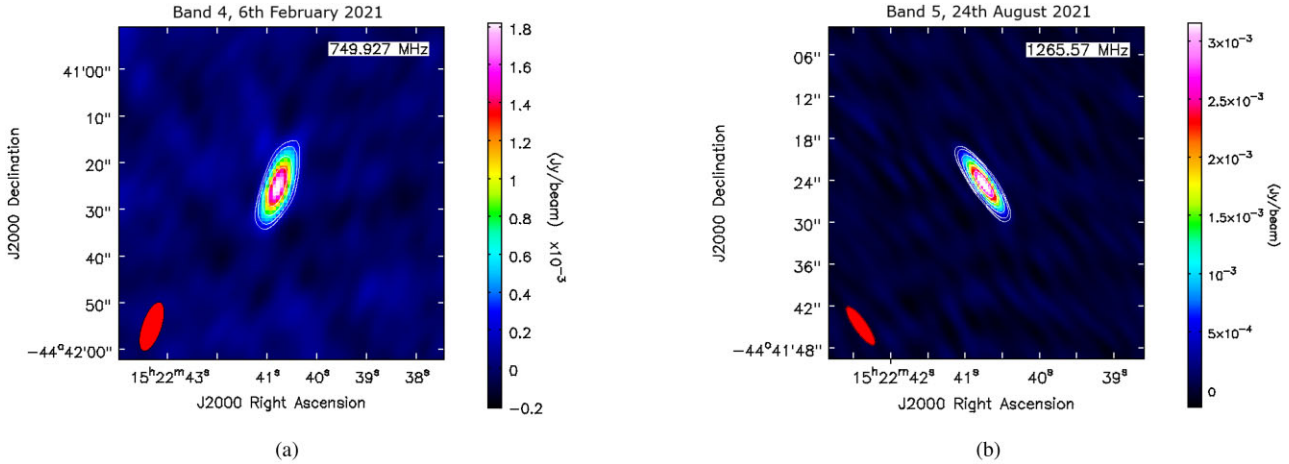


Figure 1. uGMRT continuum images of ϵ Lupi. Panel (a) shows the band 4 (550–900 MHz) detection on 2021 February 06 (orbital phase $\phi_{\text{orb}} = 0.165$) and panel (b) shows a band 5 (1050–1450 MHz) detection on 2021 August 24 ($\phi_{\text{orb}} = 0.918$). The synthesized beam is shown in red filled ellipses (size $8.37 \text{ arcsec} \times 3.09 \text{ arcsec}$ for band 4 and $7.05 \text{ arcsec} \times 1.99 \text{ arcsec}$ for band 5) at the bottom left of each plot. The contours in white show the detection significance and are drawn at 6, 10, 20, 35, 50 σ for band 4, and 6, 10, 20, 35, 50, 70 σ for band 5, where σ is the rms noise of the corresponding images near the phase center ($\sigma \sim 36 \mu\text{Jy beam}^{-1}$ for band 5 and $\sim 35 \mu\text{Jy beam}^{-1}$ for band 4).

observed to track instrumental phase and gain drifts, atmospheric and ionospheric gain, and also for monitoring the data quality for spotting occasional gain and phase jumps due to instrumental anomalies.

The data were analysed using the Common Astronomy Software Applications (CASA) package (McMullin et al. 2007). Bad channels and dead antennae were identified and flagged using the tasks ‘*plotms*’ and ‘*flagdata*’. Radio Frequency Interference (RFI) was removed by running the automatic flagging algorithm ‘*tfcrop*’ on the uncalibrated data set. The edges of the bands were flagged manually due to their low gains. We performed bandpass calibration (task ‘*bandpass*’) using the flux calibrator 3C286 to obtain frequency-dependent antenna gains, whereas to get the time-dependent gains we used the task ‘*gaincal*’. These calibrations (along with delay and flux calibration) were applied to all the sources and the corrected data were inspected. The automatic RFI excluding algorithm ‘*rflag*’ was used on the calibrated data set, and further flagging was done manually using the task ‘*flagdata*’. This flagging + calibration step was repeated cyclically until the corrected data did not show significant RFI.

The calibrated data for the target ϵ Lupi were then averaged over 4 frequency channels resulting in a final spectral resolution of 0.78 MHz. The typical final bandwidth for our observations was 290 MHz for band 4 and 370 MHz for band 5. The imaging was done using the CASA task ‘*TCLEAN*’ with deconvolver ‘*mtmfs*’ (Multiscale Multi-frequency with W-projection; Rau & Cornwell 2011). To improve the imaging quality, several rounds of phase-only and two rounds of amplitude and phase (A & P)-type self-calibration were done using the ‘*GAINCAL*’ & ‘*TCLEAN*’ tasks. Sample images of band 4 and band 5 are shown in Fig. 1. In order to inspect time-variability, these self-calibrated data sets were divided into smaller time-slices and the imaging was done for 5–15 min time slices. Table 2 reports the flux densities from images obtained by dividing each observation into several scans.

2.2 MeerKAT

We observed ϵ Lupi with MeerKAT between 2022 February 13 and 2022 March 12 under the DDT project DDT-20220120-AB-01 (PI: A. Biswas). MeerKAT is equipped with dual (linearly) polarized L

band (900–1670 MHz) and UHF band (580–1015 MHz) receivers in all the antennae. This allowed us to obtain the polarization information as well as to cover a broader wavelength range. One set of observations was performed during periastron phase spanning 5 h (Table 3), one set near the 0.75 phase (as another follow-up observation) spanning 5 h, and finally two 2-h observations were taken at two random phases (phases 0.609 and 0.526). During each observation, J1939–6342 was used as the flux calibrator, J1130–1449 was used as the polarization calibrator, and J1501–3918 was used as the gain calibrator. Similar to the uGMRT observations, sub-array mode was utilized during these observations with 32 antennae in each band. The data were recorded in full polarization mode with a bandwidth of 856 MHz divided into 4096 channels. In this paper, a detailed analysis from only the L band is discussed. The UHF band analysis will be presented in a later publication.

The data were analysed using the *processMeerKAT* script (Collier et al. 2021) available on the *ilifu*¹ cluster. To produce a reliable wideband continuum and polarization calibration, and to decrease the run-time, the script splits the band into several spectral windows (SPWs) and solves for each SPW separately. Several rounds of self-calibration steps were performed, and the final image was made using the ‘*TCLEAN*’ task in CASA. To compare the MeerKAT results with the uGMRT, the calibrated data sets were split to match the frequency range of band 5 of uGMRT. Images corresponding to different Stokes parameters (Stokes I, Q, U, and V) were then obtained. For the periastron phase, the data were imaged in smaller time ranges or single SPWs to obtain the light curve and spectra, respectively.

We noticed a nearly constant offset between the flux densities of sources in the field of view obtained from MeerKAT and uGMRT at all epochs. We selected some of the sources from the field of view for which the flux density does not vary significantly within different days obtained from the same telescope. We then obtained the mean offset value (Table A1) and corrected the MeerKAT flux density accordingly.

¹<https://www.ilifu.ac.za/>

Table 3. Observation details and imaging results of the MeerKAT observations. The bold faced phases represent periastron observations (defined by phase 0 ± 0.02). The flux-densities are not offset-corrected in this table (for all Stokes parameters).

Obs. Date	ϕ_{orb}	HJD–2459000	Band (MHz)	Stokes	Flux den. (mJy)	rms ($\mu\text{Jy beam}^{-1}$)	Pol. fraction
2022 Feb 13	0.609	623.6915 \pm 0.0306	1032–1455	I	5.581 \pm 0.045	20.84	...
			856–1717	I	5.981 \pm 0.034	25.04	...
2022 Mar 04	0.759	642.6137 \pm 0.0945	856–1717	I	5.393 \pm 0.071	14.19	...
2022 Mar 05	0.00	643.6992 \pm 0.0945	856–1717	I	5.746 \pm 0.010	14.85	...
				V	< 0.028	9.4	< 0.49 %
				Q	< 0.035	11.58	< 0.61 %
				U	0.094 \pm 0.005	9.89	1.64 \pm 0.09 %
				I	5.769 \pm 0.043	23.91	...
				V	< 0.045	15.1	< 0.78 %
				Q	< 0.041	13.82	< 0.71 %
2022 Mar 12	0.526	650.6748 \pm 0.0306	856–1717	I	3.229 \pm 0.038	23.42	...
			1032–1455	I	3.167 \pm 0.043	22.40	...

2.3 XMM–Newton

We used the archival *XMM–Newton* X-ray data for ϵ Lupi taken on 2013 March 4 (ObsID: 0690210201, PI: Y. Nazé). During the 7919 s observation, both EPIC and RGS instruments were turned on. The thick filter was used while operating in the full-frame mode of EPIC instruments and default spectroscopy mode of RGS instruments. The optical monitor (OM) was turned off as the source is optically bright.

We carried out the data reduction using the *XMM–Newton* Science Analysis System (SAS, Version: 19.1.0). The tasks ‘EMPROC’ and ‘EPPROC’ were used respectively to process EPIC-MOS and EPIC-PN data. Data were filtered by selecting events only with a pattern below 12 (for EPIC-MOS) or below 4 (for EPIC-PN). Good Time Intervals (GTI) were calculated with selection criteria: PN rate ≤ 0.4 cts sec^{-1} and MOS rate ≤ 0.35 cts sec^{-1} . After applying these GTI to our events lists, the remaining exposure times after rejecting bad data are 7.58, 7.60, and 5.60 ks for MOS 1, MOS 2, and PN, respectively. The possibility of pile-up was assessed using the task ‘EPATPLOT’ but significant pile-up was not predicted.

3 RESULTS

ϵ Lupi was detected in both uGMRT bands 4 and 5 at all observed epochs. The target was also detected with MeerKAT. The apsidal-motion corrected radio light curve together with radial velocity and B_z measurements are shown in Fig. 3. The light curve shows the presence of variable radio emission over the full phase of observation. Extreme variability is observed at band 5, characterized by the presence of enhancements of width less than ~ 0.1 orbital cycles.

The uGMRT observations covered several orbital phases (from 10 different orbits), whereas the MeerKAT observations were obtained at the periastron phase as well as 3 other orbital phases. In the MeerKAT observations, the source was detected in Stokes I flux density at all observed phases. However, the source was undetected in the Stokes Q, U, and V images at phases other than the periastron. Considering the 3σ upper limits in the respective images, the upper limits of polarization fraction for this phase are 2.07, 1.99, and 2.15 per cent, respectively for Stokes Q, U, and V. During the periastron phase, the search for polarization was done by imaging each scan separately. The source remained undetected in Stokes Q and V images, with 3σ upper limits of polarization fraction of 0.61 and 0.49 per cent. However, the source was faintly detected in Stokes U (Fig. 2) in the band 1060–1450 MHz, with flux density 118 ± 30 μJy , giving a polarization fraction of 2.05 per cent, significant at 3σ . If we consider

the whole MeerKAT L band (856–1717 MHz), the detection is at $>9\sigma$ significance. For incoherent non-thermal processes, intrinsic linear polarization reflects highly relativistic electrons and generally weak magnetic fields (Dulk 1985). It is possible that the measured fraction of linear polarization is significantly lower than the actual intrinsic polarization produced by the source. This situation may arise either due to the large beam size that may blend small components with higher polarization fractions but different field orientations, or by differential Faraday rotation and Faraday depolarization in circumstellar ionized plasma.

As mentioned above, radio data show two kinds of enhancements, short enhancements or pulses and smoothly variable possibly periodic emission. Below, we explain both in details.

3.1 Pulses in the light curve

In uGMRT band 5 data, we observe three significant enhancements (sharp jumps in the light curve): one near the periastron phase, one at phase 0.75, and another at phase 0.09 (Fig. 3). In addition, MeerKAT L band data shows enhancement at phase 0.61. No sharp enhancements are seen in the uGMRT band 4. The band 5 enhancements at periastron and at phase 0.75 are confirmed to be persistent through our subsequent re-observations of the star at the same orbital phases using both the uGMRT as well as the MeerKAT. The absence of enhancements in band 4 at the periastron phase was also confirmed by re-observing the star at a later epoch. The time-scale for the sharp enhancement observed from ϵ Lupi during the periastron phase is clearly much smaller than the orbital time-scale. Subsequent uGMRT observations (taken on 2021 July 20) acquired at phase 0.076, which is just ~ 8 h away from periastron, did not show any elevated flux density level in either band 4 or 5, reinforcing the short duration of these pulses.

To understand the nature of the enhanced radio emission, we investigated the spectral properties of the enhancements at phase 0.75 and at periastron. The periastron phase data with the uGMRT band 5 and MeerKAT L band were imaged in several smaller sub-bands to determine the nature of the emission. Between band 4 and band 5 (uGMRT data), the spectral indices at periastron and 0.75 phase are $\alpha = 1.20 \pm 0.10$ and 1.32 ± 0.06 , respectively, consistent with each other (Fig. 4a). The spectral index of the MeerKAT data during periastron ($\alpha = 1.06 \pm 0.02$) is roughly consistent with that of the uGMRT in the frequency range 1.1–1.4 GHz. The MeerKAT data also show a possible cutoff near 1 GHz (Fig. 4b).

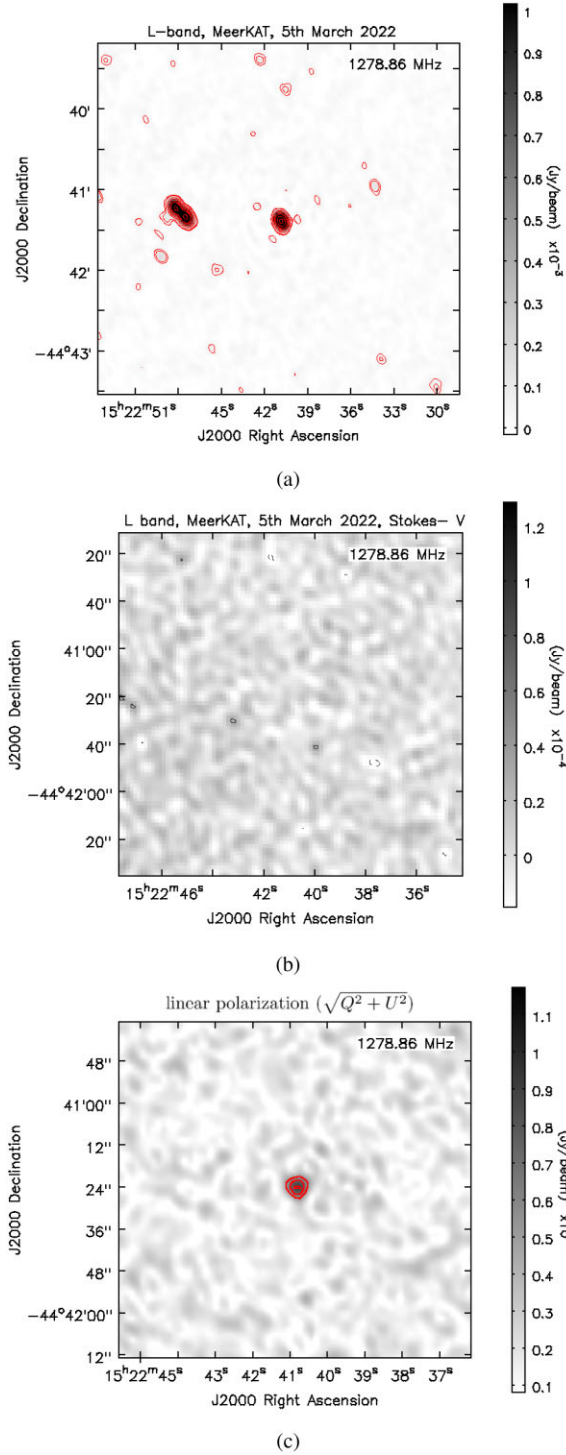


Figure 2. (a) MeerKAT L-band Stokes I image of the periastron observation on 2022 March 5. The contours in red show the detection significance and are drawn at 3, 5, 15, 30, 60, 90, 180, 300σ , where σ is the rms noise of the Stokes I image near the phase center (here, $16 \mu\text{Jy}$). (b) Stokes V image of the periastron phase showing non-detection. The rms noise in the shown Stokes V image is $\sigma \sim 9 \mu\text{Jy}$, thus constraining the upper limit of the Stokes V flux of our source to be $27 \mu\text{Jy}$. Contours are drawn at 3σ . (c) Linear polarization map obtained from Stokes Q and U images confirming the presence of linear polarization. The contours in magenta are drawn at 3, 4, 5, where $\sigma = 17 \mu\text{Jy beam}^{-1}$. The fitted peak flux from the full band is $90 \mu\text{Jy}$, showing a linear polarization fraction of 1.6 per cent.

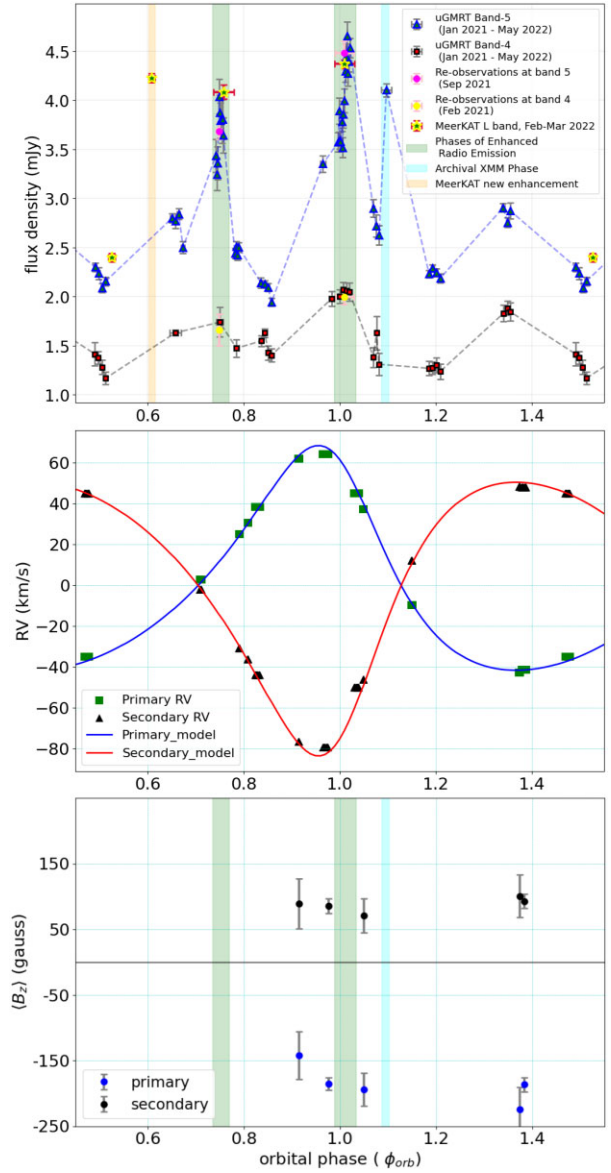


Figure 3. *Top:* radio light curve obtained with the uGMRT and MeerKAT observations. The MeerKAT flux densities are offset corrected. The repeating enhancements are highlighted with green shaded vertical bands. The cyan band represent the phase of the archival *XMM-Newton* observation and its corresponding radio follow-up; the orange band represent the enhancement at ~ 0.6 phase observed with MeerKAT. The redundant phase observations confirming the repeating nature of the flux density are shown with pink and yellow points. The yellow stars represent the MeerKAT flux densities in the uGMRT band 5 equivalent frequency range. The error bars do not include the contribution from error in the absolute flux density scale between different days of observations (~ 10 per cent), since they do not affect the inferences. *Middle:* the primary and secondary radial velocities (RVs) of ϵ Lupi from the ESPaDOnS data obtained between 2014 and 2015. Overlaid blue and red curves are the best-fitting orbital model (Pablo et al. 2019). *Bottom:* the $\langle B_z \rangle$ curve of the system showing non-detection of a magnetic null and lack of variation. The constant positive and negative $\langle B_z \rangle$ for the respective components reflects the anti-alignment of the magnetic axes (Shultz et al. 2015). Reproduced with data from Shultz et al. (2018a).

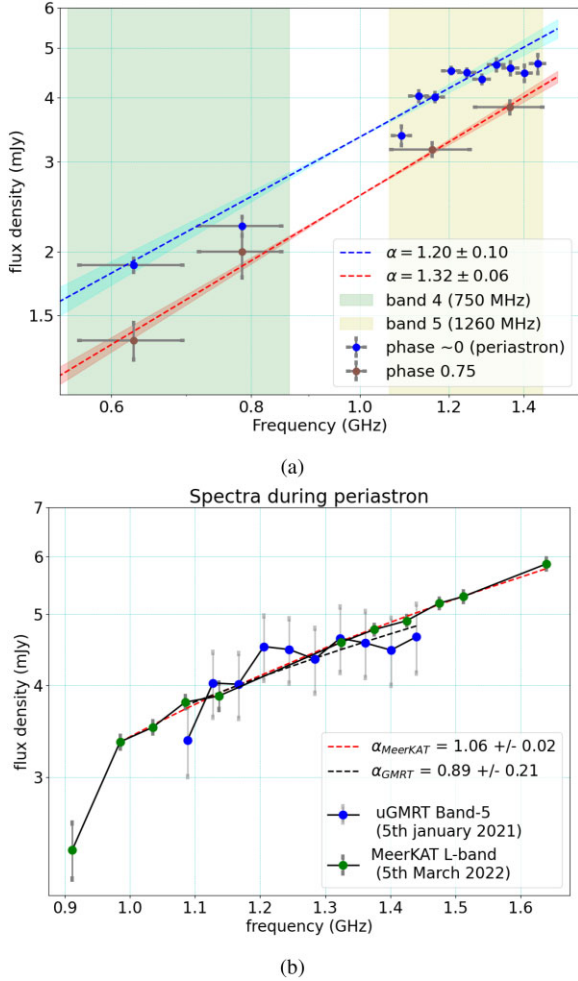


Figure 4. (a) Radio spectra of the source near the enhancement phases from uGMRT observations. The blue and red line indicate a single power-law fit to the band 5 and band 4 data points, for periastron and phase 0.75, respectively. (b) The band 5 spectra of ϵ Lupi from both uGMRT and MeerKAT during the periastron phase suggest a possible cutoff near 1 GHz.

We examined the archival *XMM-Newton* data for any possible enhancement. The background-corrected light curve from the EPIC-PN instrument is shown in Fig. 5, where we used a 100 s time-bin. The light curve is further smoothed using the 5-point moving average method. We also measured the hardness ratio between the 0.5–2 keV and 2–10 keV bands for the corresponding phases, which mimics the light curve of the total counts (Fig. 5). We discovered an enhancement in the X-ray light curve at phase ~ 0.090 . This orbital phase was followed up with uGMRT and a clear enhancement was also observed in the radio light curve in band 5 (Fig. 3, top). In a very recent study, Das et al. (2023) have reported enhancement in X-ray flux during periastron, as compared to an off-periastron phase.

3.2 Periodic variability

In addition to short enhancements at GHz band, there is a hint of periodic variability in both bands 4 and 5 uGMRT data. As the rotation periods of both components are unknown, we carried out a robust analysis of the radio flux density measurements to evaluate periodic variability. Period analysis was performed for 50 000 periods

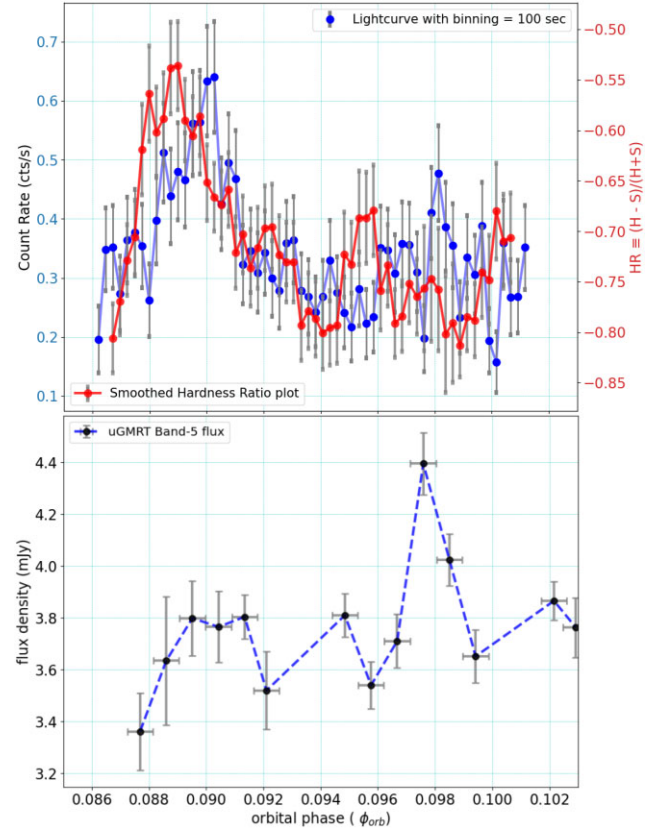
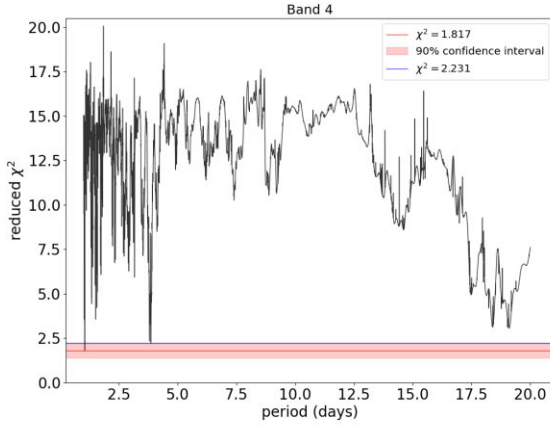


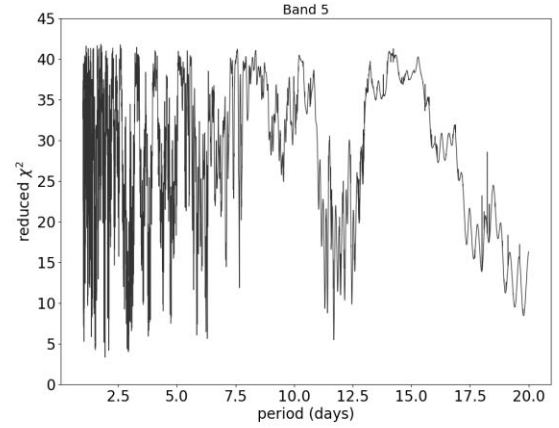
Figure 5. *Top:* the 0.2–10 keV *XMM-Newton* EPIC-PN X-ray light curve of ϵ -Lupi showing variability on short time-scales (~ 1 h). (blue:) 100-ks binned light curve. (Red:) The hardness-ratio ($HR = (H-S)/(H+S)$), where H is 2–10 keV and S is 0.2–2 keV energy ranges. The HR plot mimics the total-counts light curve. Here, phase refers to the orbital phase. *Bottom:* radio light curve obtained from the uGMRT band 5 data observed on 2022 May 26 covering the same orbital phase. The horizontal error bars represent the phase coverage of each data point. The peaks in the X-ray and radio light curves are within the phase error accumulated at the time of the observations due to the uncertainty in apsidal motion ($\Delta\phi_{orb} < 0.01$).

from 1 to 20 d, evaluating the reduced χ^2 of a sinusoidal fit to the flux density measurements phased with each period (Fig. 6). The best fit from the band 4 data yields a period of 1.052 d with a reduced χ^2 of 1.8 (Fig. 7a). Another period of 3.87 d obtained from band 4 data has slightly worse χ^2 of ~ 2.23 . As in band 4 no enhancements were found, and also, thermal emission is certain to be absorbed as evident from the free-free radius calculation (see Section C), the emission observed here is expected to be purely gyrosynchrotron coming from the individual stars. Thus the period of 1.054 d may represent the rotation period of one or both of the components (in case the components are synchronized). The band 5 data, on the other hand, yield no similar period. During the period analysis with band 5, the enhancement phases were removed as they resulted in no solution with a reduced χ^2 better than 7. Even after removing the enhancement phases, the band 5 data show poor fit due to fewer data points (Fig. 7b). Since the 1.052 d period that seems to represent the band 4 data well does not provide a satisfactory phasing of the band 5 data, the origin of this period is questionable.

Recent studies have found that non-thermal gyrosynchrotron emission from massive stars follows a scaling relation that depends on the magnetic field strength (B), rotation period (P_{rot}), and radius

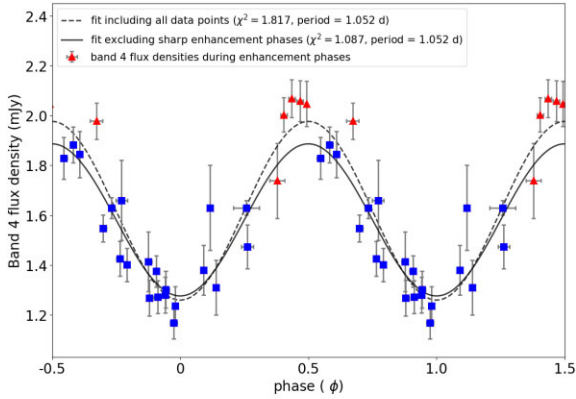


(a)

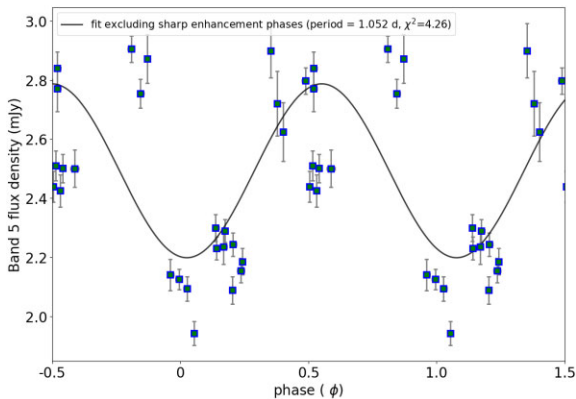


(b)

Figure 6. Reduced χ^2 distribution obtained during systematic period analysis for 50 000 periods from 1–20 d for band 4 (left) and band 5 (right) data for ϵ Lupi, respectively. The red solid horizontal line in the band 4 plot represent the $\chi^2 = 1.817$ line. The red band represent the 90 per cent confidence interval for this peak. As no significant peak was observed from band 5 data, such confidence intervals are not shown in the right image.



(a)



(b)

Figure 7. Phase-folded light curve of ϵ Lupi from GMRT data with period 1.052 d corresponding to the lowest χ^2 , (a) for band 4, with full data (red + blue) and data points excluding the enhancement phases that were observed from the band 5 observations (only blue); and (b) for band 5 data points excluding the sharp enhancement phases.

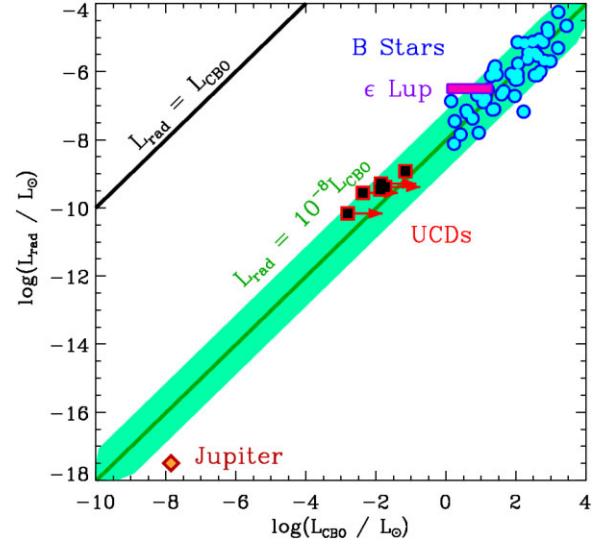


Figure 8. Plot of radio luminosity L_{rad} as a function of breakout luminosity L_{CBO} and the position of ϵ Lupi for different cases. The thick black line indicates $L_{\text{rad}} = L_{\text{CBO}}$; the solid green line shows the same line shifted so that $L_{\text{rad}} = 10^{-8} L_{\text{CBO}}$. Blue circles indicate B stars, black squares represent ultra cool dwarfs (UCDs), and the yellow diamond shaped point represent Jupiter. The data points are taken from Leto et al. (2021), and Shultz et al. (2022). The purple rectangle represent the position of ϵ Lupi in this scaling relation plot for different conditions: (a) the top of the rectangle represent the L_{rad} of ϵ Lupi during the periastron phase, while the bottom of the rectangle correspond to the basal L_{rad} of the source. (b) the rightmost point in the rectangle represent the L_{CBO} value corresponding to the period $P_{\text{rot}} = 1.052$ d, while the leftmost point of the rectangle comes if we assume $P_{\text{rot}} = P_{\text{orb}} \sim 4.56$ d.

(R) of a given star (Leto et al. 2021; Owocki et al. 2022; Shultz et al. 2022). As the radio emission scale with both the magnetic field strength and the stellar rotation rate, we plotted the position of ϵ Lupi in such scaling relationship plot for different periods and observed luminosities (Fig. 8). In such a situation, the radio emission is assumed to be gyrosynchrotron, arising according to centrifugal breakout (CBO) model (Owocki et al. 2022), in which the overall

total luminosity from CBO events (L_{CBO}) in a dipolar stellar field should follow the general scaling relation

$$L_{\text{CBO}} \approx \dot{M} \Omega^2 R_*^2 \eta_c^{1/2}, \quad (2)$$

where $\eta_c = (B_d^2 R_*^2) / (\dot{M} v_{\text{orb}})$ is the centrifugal magnetic confinement parameter, Ω is the rotational frequency, \dot{M} is the mass-loss rate, B_d is the dipolar magnetic field strength of the star, $v_{\text{orb}} = \sqrt{GM_*/R_*}$ is the near-surface orbital speed, R_* is the stellar radius, and M_* is the stellar mass. The radio luminosity (L_{rad}) in Fig. 8 is defined and calculated in a manner described by Owocki et al. (2022) from band 4 and band 5 data. The purple rectangle in Fig. 8 represents the position of ϵ Lupi in this scaling relation plot for different conditions: (a) the top of the rectangle indicates the L_{rad} of ϵ Lupi during the periastron phase, while the bottom of the rectangle correspond to the basal L_{rad} of the source. (b) the rightmost point in the rectangle indicates the L_{CBO} value corresponding to the period $P_{\text{rot}} = 1.052$ d, while the leftmost point of the rectangle comes if we assume $P_{\text{rot}} = P_{\text{orb}} \sim 4.56$ d. The basal radio luminosity is exactly consistent with the value expected for the 1.052 d period. Thus radio luminosity certainly cannot rule out the 1.052 d period as being the rotation period of one of the stars. However, as can be seen from the diagram, there is enough scatter in the relation that periods up to about the orbital period are consistent with the scaling relationship. So, we can neither confirm, nor rule out this period from the scaling relationship. However, this plot is consistent with the gyrosynchrotron nature from the basal flux.

Assuming rigid rotation and that 1.052 d is indeed the rotation period of one or both components of the system, the inclination i_{rot} of the rotational axis from the line of sight can be determined from the following equation (Stift 1976):

$$\sin i = \frac{v \sin i \cdot P_{\text{rot}}}{50.6 R_*}, \quad (3)$$

where R_* is given in units of solar radii, $v \sin i$ represents the projected rotational velocity in kms^{-1} , and P_{rot} is the rotation period in days. We use $v \sin i$ values from Shultz et al. (2018b) and for radius values, we use the range of values from Pablo et al. (2019) and Shultz et al. (2019) listed in Table 1. Adopting $P_{\text{rot}} = 1.052$ d, and assuming that this period may correspond to either the primary or the secondary, we get the inclination angles to be $8 \pm 4^\circ$ for the primary, and $8 \pm 2^\circ$ for the secondary, respectively. Statistically these low inclination angles are quite unlikely, again making this 1.052 d period questionable. Also, note that the orbital inclination (i_{orb}) is about 20° (Pablo et al. 2019). From Hut 1980, we know that the time-scale for spin-orbit alignment is very short in comparison to the circularization and tidal locking time-scales; further ϵ Lupi is a close binary, about middle aged on the main sequence. So we expect $i_{\text{orb}} = i_{\text{rot}}$. However, a 10° difference might not be impossible. A denser sampling of the radio light curve may give further insight about the rotational period.

4 DISCUSSION

We now examine the nature of radio emission from the ϵ Lupi system. We start with the possibility of radio emission being thermal in nature, produced by the ionized wind. In this case, we get the mass-loss rate using the relations reported by Bieging, Abbott & Churchwell (1989) to be $\sim 10^{-6} M_\odot \text{yr}^{-1}$. Such a high mass-loss rate is typical of very massive O-type stars and Wolf-Rayet stars, and results in strong emission lines throughout the optical spectrum in both non-magnetic and magnetic examples, which is not observed in this system (Pablo et al. 2019; Shultz et al. 2019). Furthermore, this mass-loss rate is four orders of magnitude larger than the theoretically predicted

value for stars with properties similar to those of ϵ Lupi ($\sim 0.63 \times 10^{-10} M_\odot \text{yr}^{-1}$, Vink, de Koter & Lamers 2001; Shultz et al. 2019), implying that the radio emission must be non-thermal.

Additional evidence of non-thermal radio emission comes from the brightness temperature T_B . By considering an emission site with radius as large as the half-path distance during periastron ($\sim 11.3 R_\odot$; Pablo et al. 2019), we obtain $T_B \approx 1.3 \times 10^{10}$ K. Here, we used the distance $d = 156$ pc, which was obtained from the Hipparcos parallax (van Leeuwen 2007), as reported by Pablo et al. (2019) and a flux density value of 4.6 mJy (maximum flux density during periastron). Note that, this is very likely a lower limit to the actual brightness temperature, since the actual size of the emission site is most probably smaller than assumed. The large value of T_B again points to a non-thermal emission mechanism.

As mentioned in Section 3.1, the most striking features of the radio light curve are the sharp enhancements observed at four orbital phases in band 5: nearly coinciding with periastron, at phase ≈ 0.75 , at phase ≈ 0.61 , and finally at phase ≈ 0.09 , corresponding to the X-ray enhancement. The enhancements near periastron and phase 0.75 are persistent, as confirmed by conducting multiple observations at different epochs: with the uGMRT as well as with the MeerKAT. The stability of the sharp enhancements near phases 0.09 and 0.61 cannot be confirmed as multiple observations at this phase have not been conducted. The enhancement observed at periastron is the strongest enhancement observed. The stability of the spike near phases 0.09 and 0.61 cannot be confirmed as multiple observations at this phase have not been conducted.

The characteristics of the observed sharp enhancements in the radio bands that must be satisfied by the underlying physical scenario/emission mechanism are:

- (i) The enhancements are present at four orbital phases mentioned above, one of which is the periastron phase. As the full orbital cycle was not observed, it is possible that more enhancements in the light curve will be revealed in future.
- (ii) The duration of sharp enhancements are < 0.05 orbital cycles.
- (iii) The lower limit of brightness temperature is found to be $\sim 10^{10}$ K.
- (iv) No circular polarization was detected for the periastron enhancement, but linear polarization of $\sqrt{(Q^2 + U^2)} \approx 1.6$ per cent (if the full MeerKAT L-band of 856–1717 MHz is considered, or ≈ 2.1 per cent if the uGMRT-equivalent band of 1060–1450 MHz is considered) was detected. No polarization was detected at enhancement phases.
- (v) The sharp enhancements are present only at band 5/L-band, and no enhancements were observed in band 4.
- (vi) During enhancements, between band 4 and band 5, the spectra have positive spectral indices of $\approx +1$, indicating optically thick emission.
- (vii) For the enhancement near periastron, there is a possible low-frequency cutoff at ~ 1 GHz.
- (viii) The enhancement at periastron is stronger than those observed away from periastron.
- (ix) For both persistent enhancements phases, i.e. at periastron and at phase 0.75, multiple observations yield similar flux densities at different epochs.

Characteristics (ii) to (v) give the strongest constraints regarding the radiative processes. The possible underlying physical scenarios can be divided into two cases:

Case I: The underlying physical process is triggered only at certain orbital phases, and lasts for a short time (which determines the duration of the enhancements).

The relevant processes meeting this criteria could be gyrosynchrotron, synchrotron and/or plasma emission, triggered by either magnetic reconnection or shocks due to wind–wind collision. The high brightness temperature makes the gyrosynchrotron process unlikely (Robinson 1978). The presence of stable ~ 1.6 per cent linear polarization across the periastron observation indicates that a quite energetic electron population is present. Such a high brightness temperature, the presence of linear polarization, and the absence of circular polarization points towards synchrotron emission. Furthermore, repetitive behaviour of these enhancements around the periastron phase suggests a role for binarity. In the following subsection (Section 4.1), we investigate the possibility of synchrotron emission from binary interaction: either due to wind–wind collision or as a result of magnetic reconnection as the underlying physical process for the sharp enhancements in band 5/L band.

Case II: The underlying physical process is present at all times, but the resulting emission is observable only at certain orbital phases.

For the second type of interaction, there are again two possibilities. The first is that the emission site is not visible to the observer at all orbital phases. However, the fact that the system is viewed nearly ‘face-on’, with the rotational inclination angles of the individual stars likely equal (or possibly even smaller, if the 1.052 d period is rotational) to the small orbital inclination (Shultz et al. 2015; Pablo et al. 2019) makes this possibility unlikely, because our view of the system geometry does not change significantly during an orbit. The remaining possibility for the second kind of interaction is that the emission is highly directed, in which case the relevant emission mechanism is electron cyclotron maser emission (ECME). In Section 4.2, we investigate the possibility of ECME in detail.

4.1 Case I: synchrotron origin of the radio enhancements at periastron

Synchrotron emission can arise due to two mechanisms: (1) particles accelerated in shocks created via wind–wind collisions due to proximity of the stars, and/or (2) particles accelerated via magnetic reconnection.

Wind–wind collision is not very likely in B-star binaries, as due to their low mass-loss rates, the winds are not sufficiently strong to produce enhancements in a short period of time. However, in the case of ϵ Lupi, the proximity during periastron may cause high-density confined winds inside the magnetospheres to collide, resulting in a shorter phase enhancement of synchrotron emission because of the small zone in which winds are interacting. The archival X-ray observations can already give some hints in this scenario. Empirically, the ratio between L_x and L_{BOL} for a single main sequence non-magnetic B star is about 10^{-7} (Berghoefer et al. 1997; De Becker 2007; Nazé et al. 2014), where L_x and L_{BOL} are the X-ray and bolometric luminosities, respectively. The ratio can be larger in the presence of a magnetic field as X-rays are produced by magnetically confined wind shocks (Babel & Montmerle 1997; ud-Doula et al. 2014). Any strong excess with respect to this ratio could be explained as an interaction between stellar winds in a binary system. From the X-ray spectrum, Nazé et al. (2014) found for ϵ Lupi, the value of $\log(L_x/L_{\text{BOL}})$ to be -7.16 ± 0.02 . In this case, the relatively low ratio of the two luminosities close to periastron ($\phi_{\text{orb}} < 0.1$) suggests that the X-ray emission is consistent with that seen for solitary magnetic massive stars, and possibly indicates the lack of strong wind–wind interaction. Densely sampled X-ray observations will be critical for evaluating this scenario.

The other possibility is magnetic reconnection. As mentioned earlier, Shultz et al. (2015) predicted the overlapping of the Alfvén

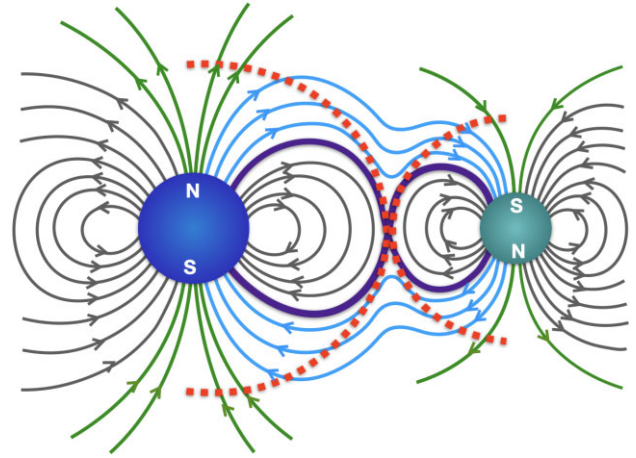


Figure 9. Schematic diagram of magnetic field lines for an ϵ Lupi-like interacting short period binary system where the components have anti-aligned dipole fields. The dark grey lines represent closed magnetic field lines, and the green lines represent open magnetic field lines. The blue solid lines are the ones that start on one star and close on the other. The purple solid curves mark the boundary between the field lines that close on the same star from which they originate and those that extend to the other star. At their crossing, the magnetic field strength \mathbf{B} vanishes. The dotted red semi-circles represent the Alfvén radii (R_A).

surfaces of the two components throughout the orbital cycle, resulting in strong magnetic reconnection. The magnetospheres of the components in ϵ Lupi are guaranteed to collide. Due to the eccentric orbit, the magnetospheres of the two stars are further squeezed near periastron (Fig. 9), resulting in magnetic reconnection being strongest during periastron. This can produce recurrent enhancements in the light curve. In this scenario, the observed emission will arise from the change in energy stored in the composite magnetic field of the system. The enhancements in radio emission during periastron phases of binary systems were previously observed in some proto-star systems, which were attributed to synchrotron emission driven by reconnection due to binary-magnetospheric interaction (e.g. Massi, Menten & Neidhöfer 2002; Massi et al. 2006; Salter et al. 2010; Adams et al. 2011). Note that, these systems differ from ϵ Lupi in one important aspect, which is that unlike ϵ Lupi, the Alfvén surfaces of the binary components of the proto-star systems do not overlap at all orbital phases. Nevertheless, the oppositely aligned magnetic fields of the two components of ϵ Lupi certainly favour the magnetic reconnection scenario (e.g. Adams et al. 2011). The associated energy release may produce non-thermal electrons which can then emit synchrotron radiation.

However, one of the major challenges in this scenario is explaining the absence of enhancements in band 4. Non-thermal radio emission can be absorbed by three processes: synchrotron self-absorption, free–free absorption, and Razin suppression. The absence of a band 4 enhancement indicates a sharp decrease of emission with frequency, ruling out synchrotron self-absorption. While free–free absorption is exponential in nature and band 4 absorption will be higher than that in band 5, it cannot account for the complete absence of sharp enhancements in band 4 (see Appendix C).

Razin suppression (Rybicki & Lightman 1979; Dougherty et al. 2003; Erba & Ignace 2022) can lead to the suppression of lower frequency emission, and keep the frequency of maximum brightness temperature constant (see Appendix B for details). Razin suppression of the synchrotron emission will scale as $\approx e^{-\nu_R/\nu}$, where ν_R is the

Razin frequency which scales as n_e/B (Appendix B). Taking 1 GHz as the cutoff frequency, we get the number density to be $1.5 \times 10^9 \text{ cm}^{-3}$ (for $B = 30 \text{ G}$, magnetic field along equator $\sim B_0/2r^3$). Such high densities are possible because the collision of magnetically confined wind plasma implies the compression of that plasma. For the out-of-periastron enhancements, both n_e and B will be smaller, which may explain observing a similar cutoff at other orbital phases. Thus Razin suppression is quite a plausible mechanism to explain the absence of enhancements in band 4.

4.2 Case II: electron cyclotron maser emission origin of the radio enhancements at periastron

In this section, we consider the second possibility: the coherent Electron Cyclotron Maser Emission (ECME) mechanism (for details, see Appendix D), produced by mildly relativistic electrons with an unstable energy distribution, provided the local electron gyrofrequency ω_B is larger than the corresponding plasma frequency ω_p (e.g. Treumann 2006). For hot magnetic stars, ECME pulses are expected to be visible close to the magnetic null phases (e.g. Trigilio et al. 2000).

In the case of ϵ Lupi, there are two issues for the ECME origin of radio emission: (1) the orientations of the stellar rotation and magnetic axes are such that the magnetic nulls are never visible for any of the star. (2) No circular polarization was detected for the enhanced radio emission. The lack of circular polarization presents an obvious problem for the ECME scenario, since ECME is generally highly circularly polarized (e.g. Melrose & Dulk 1982). However, the two stars have similar (albeit not identical) surface magnetic fields which are anti-aligned. This configuration could result in the circular polarization of the ECME pulses cancelling out. Nearly zero circular polarization for ECME pulses was indeed observed for some hot magnetic stars (e.g. Das et al. 2022b). However, this requires a large degree of fine-tuning, and it is unlikely that the circular polarization is perfectly cancelled. Rather, there would likely be some residual circular polarization, which might well fall below the sensitivity threshold, especially given the likelihood of absorption within the stellar wind plasma.

The first difficulty may also be resolved if we consider that ECME production in this system is different from that for solitary magnetic stars where the emission is believed to be produced in auroral rings in an azimuthally symmetric manner (Trigilio et al. 2011). In the case of ϵ Lupi, ECME is likely triggered by binary interaction, such as magnetic reconnections at the regions where the two magnetospheres overlap. This naturally removes the magnetic azimuthal symmetry of ECME production. This scenario is then more aligned with the active longitude scenario (e.g. Kuznetsov et al. 2012) where only a set of magnetic field lines participate in the ECME production, and the emission is directed along the hollow cone surfaces (of half opening angle of $\approx 90^\circ$) centred at these field lines.

We show in Appendix D that under the scenario that a given magnetic field line is ‘activated’ due to the perturbation from the companion star, the ECME in bands 5 and 4 are not necessarily observable at the same rotational phase. Besides, even for the cases where ECME at both frequencies are observable at the same rotational phase, the magnetic field lines involved are not necessarily the same. Thus, the non-observation of ECME in band 4 could either be due to not being able to observe the star at the right rotational phase, or that the magnetic field lines that are required to produce ECME at band 4 are not ‘activated’ (the ones that come in contact with the secondary’s magnetosphere). However, we note that since the visibility of the pulses is also dependent on the rotational phase,

the ECME scenario will be relevant only if the rotational frequencies are harmonics of the orbital frequency.

4.3 Presence of other enhancements

So far, we have primarily discussed the enhancement at the periastron phase. However, the uGMRT observation revealed a second persistent peak, separated from periastron by ~ 0.25 cycles or by $\sim 27.3 \text{ h}$. Further observation suggested a third peak near the same phase where the possible X-ray enhancement is observed, and finally a MeerKAT observation suggested a fourth peak at phase 0.61. Although the repeating enhancements during periastron can be explained as an effect of magnetospheric interaction via reconnection, with emission mechanism being either synchrotron or ECME, the origins of the other enhancements are not clear.

As we do not have information about the individual rotation periods, we cannot conclude whether the stars have the same rotation periods. If they are not synchronized, further enhancements can be caused by magnetic reconnection phenomena due to the relative motion of the magnetospheres (Gregory et al. 2013). The possible enhancement seen in the X-ray light curve can also have any of the origins stated above. A dense sampling of orbital phase is thus necessary to fully characterize the variability of the system. Also, due to very slow overall winding of the coupled magnetic fields of the magnetically coupled system, magnetic energy is gradually accumulated, which may be eventually released in a flare when the instability threshold is reached (Cherkis & Lyutikov 2021). Such a scenario is possible in this system. If the rotation period is a harmonic of the orbital period, ECME can be a plausible mechanism to produce such flares.

5 CONCLUSION

In this work, we report the discovery of GHz and sub-GHz emission from the close magnetic binary ϵ Lupi. This is the only known main-sequence binary system to show direct evidence of magnetospheric interaction. The star is detected in both band 4 (550–950 MHz) and band 5 (1050–1450 MHz) of uGMRT and the L band (900–1670 MHz) of MeerKAT at all observing epochs.

The most striking feature of the radio light curve is the existence of sharp radio enhancements at four orbital phases: One during the periastron phase and three others at orbital phases 0.09, 0.61, and 0.75 in bands $> 1 \text{ GHz}$. The enhancement at phase ~ 0.09 is also coincident with the enhancement seen in the archival *XMM-Newton* data. MeerKAT data reveal 1.6–2.1 per cent Stokes U polarization during periastron.

We propose that magnetic reconnection is the most favourable scenario for accelerating electrons during periastron. The non-thermal sharply enhanced radio emission can possibly arise via two mechanisms:

(i) *Synchrotron emission suppressed below 1 GHz via Razin suppression.* In this scenario, especially during periastron, strong magnetic reconnection may take place due to proximity, and recurrent emission may arise from the change in energy stored in the composite magnetic field of the system.

(ii) *Coherent electron cyclotron maser emission with lower cutoff 1 GHz.* In this scenario, certain magnetic field lines are ‘activated’ due to the perturbation from the companion star, making ECME observable at different rotational phases at different frequencies. However, this scenario required serious fine tuning.

The basal emission is consistent with being gyrosynchrotron in nature. We find periodic variability in the basal radio emission with a ~ 1.052 d period. However, it remains inconclusive whether this represents the rotation period of one or both stars in the system.

While the nature of both the periodic variability of the basal flux and the recurring sharp flux enhancements remain to be determined, these patterns of variation appear to be unique among magnetic hot stars, and are almost certainly related to ϵ Lupi's status as the only known doubly magnetic hot binary. These tantalizing indications that the system's magnetospheres are in fact overlapping establish ϵ Lupi as a test system for the physics of magnetospheric binary stars.

ACKNOWLEDGEMENTS

We thank the referee for their detailed and valuable comments. AB and PC acknowledge support of the Department of Atomic Energy, Government of India, under project no. 12- R&D-TFR-5.02-0700. B.D. acknowledges support from the Bartol Research Institute. GAW acknowledges support in the form of a Discovery Grant from the Natural Sciences and Engineering Research Council (NSERC) of Canada. MES acknowledges the financial support provided by the Annie Jump Cannon Fellowship, supported by the University of Delaware and endowed by the Mount Cuba Astronomical Observatory. The GMRT is run by the National Centre for Radio Astrophysics of the Tata Institute of Fundamental Research. The MeerKAT telescope is operated by the South African Radio Astronomy Observatory, which is a facility of the National Research Foundation, an agency of the Department of Science and Innovation. The National Radio Astronomy Observatory is a facility of the National Science Foundation operated under cooperative agreement by Associated Universities, Inc. Part of this work was carried out using the data processing pipelines developed at the Inter-University Institute for Data Intensive Astronomy (IDIA) and available at <https://idia-pipelines.github.io>. IDIA is a partnership of the University of Cape Town, the University of Pretoria and the University of the Western Cape.

DATA AVAILABILITY

The uGMRT data used in this work is available from the GMRT online archive (<https://naps.ncra.tifr.res.in/goa/data/search>). The *XMM-Newton* data are available from the *XMM-Newton* Science Archive (XSA) (<https://www.cosmos.esa.int/web/xmm-newton/xsa>). The MeerKAT data can be found in SRAO MeerKAT archive (see <https://skafrica.atlassian.net/servicedesk/customer/portal/1/article/302546945>). The analysed data are available upon request to the corresponding author.

REFERENCES

Abbott B. P. et al., 2016a, *Phys. Rev. Lett.*, 116, 061102
 Abbott B. P. et al., 2016b, *Phys. Rev. Lett.*, 116, 241103
 Adams F. C., Cai M. J., Galli D., Lizano S., Shu F. H., 2011, *ApJ*, 743, 175
 Alecian E. et al., 2015, *Proc. Int. Astron. Un.*, 9, 330
 Andre P., Montmerle T., Feigelson E. D., Stine P. C., Klein K.-L., 1988, *ApJ*, 335, 940
 Babel J., Montmerle T., 1997, *A&A*, 323, 121
 Belkora L., 1996, in Ramaty R., Mandzhavidze N., Hua X.-M., eds, ASP Conf. Ser. Vol. 374, High energy solar Physics. Astron. Soc. Pac., San Francisco, p. 416
 Berghoefer T. W., Schmitt J. H. M. M., Danner R., Cassinelli J. P., 1997, *A&A*, 322, 167
 Biegging J. H., Abbott D. C., Churchwell E. B., 1989, *ApJ*, 340, 518

Campbell W. W., Moore J. H., 1928, *Publ. Lick Obs.*, 16, 223
 Chandra P. et al., 2015, *MNRAS*, 452, 1245
 Cherkis S. A., Lyutikov M., 2021, *ApJ*, 923, 13
 Collier J. D., Frank B., Sekhar S., Taylor A. R., 2021, in "The IDIA PROCESSMEERKAT pipeline: Fast CASA Processing on a Cloud-Based HPC Cluster," 2021 XXXIVth General Assembly and Scientific Symposium of the International Union of Radio Science (URSI GASS). Rome, Italy, p. 1
 Das B., Chandra P., 2021, *ApJ*, 921, 9
 Das B., Mondal S., Chandra P., 2020, *ApJ*, 900, 156
 Das B., Chandra P., Petit V., 2022a, *MNRAS*, 515, 2008
 Das B., Chandra P., Shultz M. E., Leto P., Mikulášek Z., Petit V., Wade G. A., 2022b, *MNRAS*, 517, 5756
 Das B. et al., 2022c, *ApJ*, 925, 125
 Das B. et al., 2023, *MNRAS*, 522, 5805
 De Becker M., 2007, *A&A Rev.*, 14, 171
 Dougherty S. M., Pittard J. M., Kasian L., Coker R. F., Williams P. M., Lloyd H. M., 2003, *A&A*, 409, 217
 Dulk G. A., 1985, *ARA&A*, 23, 169
 El'kin V. G., 1999, *Astron. Lett.*, 25, 809
 Erba C., Ignace R., 2022, *ApJ*, 932, 10
 Erba C. et al., 2021, *MNRAS*, 506, 5373
 Ginzburg V. L., Syrovatskii S. I., 1965, *ARA&A*, 3, 297
 Gregory S. G. et al., 2013, *Proc. Int. Astron. Un.*, 9, 44
 Grunhut J. H. et al., 2017, *MNRAS*, 465, 2432
 Gupta Y. et al., 2017, *Curr. Sci.*, 113, 707
 Hut P., 1980, *A&A*, 92, 167
 Izzard R. G., Dray L. M., Karakas A. I., Lugaro M., Tout C. A., 2006, *A&A*, 460, 565
 Jonas J. L., 2009, *IEEE Proc.*, 97, 1522
 Karmakar S., Naik S., Pandey J. C., Savanov I. S., 2023, *MNRAS*, 518, 900
 Keszthelyi Z., Meynet G., Georgy C., Wade G. A., Petit V., David-Uraz A., 2019, *MNRAS*, 485, 5843
 Keszthelyi Z. et al., 2020, *MNRAS*, 493, 518
 Kuznetsov A. A., Doyle J. G., Yu S., Hallinan G., Antonova A., Golden A., 2012, *ApJ*, 746, 99
 Leto P., Trigilio C., Buemi C. S., Umana G., Ingallinera A., Cerrigone L., 2016, *MNRAS*, 459, 1159
 Leto P. et al., 2021, *MNRAS*, 507, 1979
 Linsky J. L., Drake S. A., Bastian T. S., 1992, *ApJ*, 393, 341
 Massi M., Menten K., Neidhöfer J., 2002, *A&A*, 382, 152
 Massi M., Forbrich J., Menten K. M., Torricelli-Ciamponi G., Neidhöfer J., Leurini S., Bertoldi F., 2006, *A&A*, 453, 959
 McMullin J. P., Waters B., Schiebel D., Young W., Golap K., 2007, in Shaw R. A., Hill F., Bell D. J., eds, ASP Conf. Ser. Vol. 376, Astronomical Data Analysis Software and Systems XVI. Astron. Soc. Pac., San Francisco, p. 127
 Melrose D. B., Dulk G. A., 1982, *ApJ*, 259, 844
 Moore J. H., 1911, *Lick Obs. Bull.*, 6, 150
 Most E. R., Philippov A. A., 2023, *Phys. Rev. Lett.*, 130, 245201
 Most E. R., Philippov A. A., 2022, *MNRAS*, 515, 2710
 Nazé Y., Petit V., Rinbrand M., Cohen D., Owocki S., ud-Doula A., Wade G. A., 2014, *ApJS*, 215, 10
 Oksala M. E., Grunhut J. H., Kraus M., Borges Fernandes M., Neiner C., Condori C. A. H., Campagnolo J. C. N., Souza T. B., 2015, *A&A*, 578, A112
 Owocki S. P., Shultz M. E., ud-Doula A., Chandra P., Das B., Leto P., 2022, *MNRAS*, 513, 1449
 Pablo H. et al., 2019, *MNRAS*, 488, 64
 Petit V. et al., 2013, *MNRAS*, 429, 398
 Petit V. et al., 2017, *MNRAS*, 466, 1052
 Rau U., Cornwell T. J., 2011, *A&A*, 532, A71
 Robinson R. D., 1978, *Aust. J. Phys.*, 31, 547
 Rybicki G. B., Lightman A. P., 1979, Radiative processes in astrophysics. Wiley-Interscience, New York
 Salter D. M., Kóspál Á., Getman K. V., Hogerheijde M. R., van Kempen T. A., Carpenter J. M., Blake G. A., Wilner D., 2010, *A&A*, 521, A32
 Sana H. et al., 2012, *Sci.*, 337, 444

- Semenko E. A., Kichigina L. A., Kuchaeva E. Y., 2011, *Astron. Nachr.*, 332, 948
- Shultz M., Wade G. A., Alecian E., *BinaMicS Collaboration* 2015, *MNRAS*, 454, L1
- Shultz M. et al., 2018a, VizieR On-line Data Catalog: J/MNRAS/513/1429., Originally published in: 2022MNRAS.513.1429S
- Shultz M., Rivinius T., Wade G. A., Alecian E., Petit V., *BinaMicS Collaboration* 2018b, *MNRAS*, 475, 839
- Shultz M. E. et al., 2019, *MNRAS*, 490, 274
- Shultz M. E. et al., 2020, *MNRAS*, 499, 5379
- Shultz M. E., Rivinius T., Wade G. A., Kochukhov O., Alecian E., David-Uraz A., Sikora J., 2021, *MNRAS*, 504, 4850
- Shultz M. E. et al., 2022, *MNRAS*, 513, 1429
- Sikora J., Wade G. A., Power J., Neiner C., 2019, *MNRAS*, 483, 3127
- Stift M. J., 1976, *A&A*, 50, 125
- Swarup G., 1992, *Acta Astron.*, 26, 239
- Thackeray A. D., 1970, *MNRAS*, 149, 75
- Tofflemire B. M., Mathieu R. D., Ardila D. R., Akeson R. L., Ciardi D. R., Johns-Krull C., Herczeg G. J., Quijano-Vodniza A., 2017, *ApJ*, 835, 8
- Torres D., Rea N., eds, 2011, Proceedings of the First Session of the Sant Cugat Forum on Astrophysics, High-Energy Emission from Pulsars and their Systems. Springer, New York
- Townsend R. H. D., Owocki S. P., 2005, *MNRAS*, 357, 251
- Treumann R. A., 2006, *A&A Rev.*, 13, 229
- Trigilio C., Leto P., Leone F., Umama G., Buemi C., 2000, *A&A*, 362, 281
- Trigilio C., Leto P., Umama G., Buemi C. S., Leone F., 2011, *ApJ*, 739, L10
- ud-Doula A., Owocki S. P., 2002, *ApJ*, 576, 413
- ud-Doula A., Sundqvist J. O., Owocki S. P., Petit V., Townsend R. H. D., 2013, *MNRAS*, 428, 2723
- ud-Doula A., Owocki S., Townsend R., Petit V., Cohen D., 2014, *MNRAS*, 441, 3600
- Uchida Y., Sakurai T., 1983, in Byrne P. B., Rodono M., eds, Astrophysics and Space Science Library Vol. 102, IAU Colloq. 71: Activity in Red-Dwarf Stars. Springer-Verlag, Berlin, p. 629
- Uyterhoeven K., Harmanec P., Telting J. H., Aerts C., 2005, *A&A*, 440, 249
- van Leeuwen F., 2007, Hipparcos, the New Reduction of the Raw Data, 0067-0057 Vol. 350. Springer, Berlin
- Vink J. S., de Koter A., Lamers H. J. G. L. M., 2001, *A&A*, 369, 574
- Wade G. A. et al., 2014, *Proc. Int. Astron. Un.*, 9, 265
- Wang J.-S., Peng F.-K., Wu K., Dai Z.-G., 2018, *ApJ*, 868, 19
- Weiss W. W. et al., 2014, *PASP*, 126, 573

APPENDIX A: FLUX-SCALE MISMATCH

We noticed a nearly constant offset between the flux densities of sources in the field of view obtained from MeerKAT and uGMRT. We selected some of the sources from the field of view for which the flux density does not vary significantly within different days obtained from a same telescope. We selected the MeerKAT periastron observation on 2022 March 05, and uGMRT periastron observation on 2021 January 05 to compare the flux densities. We then obtained the mean offset value (Table A1) and reduced the MeerKAT flux accordingly. It should be noted that (i) the flux densities of these test sources do not vary significantly among observations with the same telescope, (ii) the flux densities of the uGMRT flux calibrators

Table A1. Flux densities of other sources from the MeerKAT periastron observation on 2022 March 05, and uGMRT periastron observation on 2021 January 05. The mean offset ratio is 0.75719.

RA	DEC	uGMRT Flux Den.	MeerKAT Flux Den.	Ratio (uGMRT/MeerKAT)
15:22:36.3	−44:45:09.4	1.163 ± 0.048	1.670 ± 0.031	0.69641 ± 0.03152
15:23:07.5	−44:42:32.4	0.636 ± 0.048	0.801 ± 0.041	0.79401 ± 0.07241
15:23:18.8	−44:44:07.9	1.506 ± 0.061	2.385 ± 0.040	0.63145 ± 0.02768
15:22:38.2	−44:45:30.7	0.630 ± 0.061	0.653 ± 0.037	0.96478 ± 0.10823
15:22:04.4	−44:42:36.4	0.397 ± 0.049	0.565 ± 0.025	0.70265 ± 0.09213
15:23:40.5	−44:37:04.3	2.630 ± 0.110	3.684 ± 0.043	0.71390 ± 0.03100
15:23:43.3	−44:37:50.3	2.462 ± 0.099	3.258 ± 0.058	0.75568 ± 0.03323
15:23:36.3	−44:38:44.2	1.587 ± 0.082	2.223 ± 0.038	0.71390 ± 0.03885
15:23:31.2	−44:40:36.2	1.054 ± 0.066	1.958 ± 0.033	0.53830 ± 0.03491
15:21:58.4	−44:40:46.1	0.818 ± 0.057	0.748 ± 0.035	1.09358 ± 0.09179
15:23:23.7	−44:33:18.2	0.961 ± 0.074	1.298 ± 0.040	0.74037 ± 0.06141
15:23:18.9	−44:47:31.9	0.788 ± 0.060	1.063 ± 0.045	0.74130 ± 0.06458

were in agreement with the VLA calibrator manual,² and (iii) The MeerKAT *L*-band flux densities of all sources from our analysis matched well with the results of MeerKAT's SDP pipeline products available in MeerKAT archive. The reason behind this constant flux-scale offset is not yet known, and we plan to address this issue in future publications.

APPENDIX B: RAZIN SUPPRESSION

Razin suppression (e.g. Rybicki & Lightman 1979; Dougherty et al. 2003; Erba & Ignace 2022) is basically the suppression of radiation whose refractive index is <1 in a given medium. This effect has been used to explain the spectra of solar microwave bursts and their steep slopes at lower frequencies. Belkora (1996) used the Razin suppression effect to explain the solar burst spectrum of 1992 July 16 taken with the Owens Valley Solar Array. They used the X-ray data of the flare to show that free-free absorption may be present, but is inadequate to explain the shape and evolution of the spectra. They found that the Razin effect not only leads to the suppression of lower frequency emission, but the frequency of maximum brightness temperature also remains constant.

Here, we attempt to explain the effect of Razin suppression and its possible role in the low-frequency cutoff near ~ 1 GHz. The presence of plasma in the emitting region means that the phase velocity of light in the medium is c/n_r , where n_r is the refractive index, which decreases towards low frequencies. As a result, synchrotron radiation is reduced at lower frequencies due to suppression of the beaming effect responsible for synchrotron radiation. The consequence is a low-frequency cutoff near the Razin frequency (ν_R) given by Ginzburg & Syrovatskii (1965):

$$\nu_R = 2 \times 10^{-8} \frac{n_e}{B} \text{ GHz}, \quad (\text{B1})$$

where n_e is the electron density in cm^{-3} , and B is the magnetic field strength in G. The suppression of the synchrotron emission scales as $\approx e^{-\nu_R/\nu}$. Taking 1 GHz as the cutoff frequency and 59 G as the magnetic field strength, we get the number density to be $2.95 \times 10^9 \text{ cm}^{-3}$. As the magnetospheres will collide during periastron, the winds confined in the components can reach such high densities. For the out-of-periastron enhancements, both n_e and B will be smaller, which may explain observing a similar cutoff at other orbital phases. Thus Razin suppression is quite a plausible mechanism in determining the structure of the radio enhancements in ϵ Lupi.

This effect can also explain the positive spectral index observed in this case. In a sufficiently steep distribution of relativistic electrons, Razin suppression of the synchrotron emission becomes more pronounced. This in turn may produce a spectral energy distribution with a power-law slope that mimics the result for thermal emission, particularly in a given waveband (Erba & Ignace 2022).

APPENDIX C: FREE-FREE ABSORPTION

To investigate the role of free-free absorption (FFA), we calculated intra-band radio spectra for both bands during periastron phase and phase 0.75. The band 5 intra-band spectral index is smaller than that in band 4, as well as between band 4 and band 5 (Fig. 4). This is expected if absorption is important. The radius of the free-free radio photosphere (R_{ff} , the distance from the star where the free-free

optical depth $\tau_{\text{ff}} = 1$) can be calculated using Torres & Rea (2011) as:

$$\tau_{\text{ff}} = 5 \times 10^3 \dot{M}_{-8}^2 V_{\infty'}^{-1} \nu^{-2} T_{\text{wind}}^{-3/2} D_{\text{ff}}^{-3}, \quad (\text{C1})$$

where, \dot{M}_{-8} is the mass-loss rate in units of $10^{-8} M_{\odot} \text{ yr}^{-1}$, $V_{\infty'}$ is the terminal velocity in units of 10^8 cm s^{-1} , ν is the frequency of observation in GHz, T_{wind} is the wind temperature in units of 10^5 K , and D_{ff} is the distance from the star, in units of $3 \times 10^{12} \text{ cm}$. When $\tau_{\text{ff}} = 1$, $D_{\text{ff}} = R_{\text{ff}}$. Taking the theoretical mass-loss value ($\sim 0.63 \times 10^{-10} M_{\odot} \text{ yr}^{-1}$; Shultz et al. 2019), we calculate the free-free radius assuming the parameters $V_{\infty'} = 2004 \text{ km s}^{-1}$, and $T_{\text{wind}} \sim T_{\text{eff}}/2 = 11 \text{ kK}$. For band 4, we get $R_{\text{ff}} \sim 15.7 R_*$ and for band 5, we get $R_{\text{ff}} \sim 11.2 R_*$, taking a radius of $4.64 R_{\odot}$ (Pablo et al. 2019) for the primary.

Adopting the lower limit value of R_A of the primary star to be $\sim 11 R_*$ (Shultz et al. 2019), we get the ratio $R_{\text{ff}}/R_A \sim 1.4$ for band 4 and ~ 1 for band 5. $R_{\text{ff}} > R_A$ signifies that the magnetospheric emission will be hidden within the radio photosphere of the wind, i.e. most of the non-thermal emission will be absorbed. This supports our assumption of heavy free-free absorption in band 4 but not completely in band 5. Although this ratio is higher than most B-type stars (Chandra et al. 2015), due to large uncertainties in the mass-loss and other parameters, this value is not too significant. The fact that more absorption is expected in band 4 remains true irrespective of the uncertainties. While free-free absorption may play an important role, it cannot be solely responsible for the absence of enhancements in band 4.

APPENDIX D: ECME

ECME gives rise to highly circularly polarized (~ 100 per cent) emission, directed almost perpendicular to the local magnetic field direction (e.g. Melrose & Dulk 1982). The frequency of emission is proportional to the local ω_B , which results in the fact that in a stellar magnetosphere, higher frequencies are produced closer to the star (where the magnetic field is stronger) and vice-versa. In this section, we aim to investigate whether there are any circumstances under which ECME emitted at a right angle to the local magnetic field lines can explain the observed radio emission from the ϵ Lupi system. Considering the similarity between the two components, we perform our calculations for only the primary star. Also, we assume that only one of the magnetic hemispheres (that facing the line-of-sight) is relevant in terms of production of *observable* ECME.

We first define a co-ordinate frame for the star under consideration (the primary star). We define the plane passing through its rotation and magnetic axes as the X-Z plane (left of Fig. D1). Thus the magnetic field line intersecting the rotation axis has longitude $\phi_B = 0^\circ$. Let us assume that ECME is produced along a magnetic field line with longitude $\phi_B = \phi_{B0}$, and with maximum radius L (see right of Fig. D1), such that the radial and polar (θ) coordinates of the points lying along the field line are related as:

$$r = L \sin^2 \theta \quad (\text{D1})$$

Let 'P' be the point at which ECME at frequency ν is produced, and emitted at an angle 90° . Our aim is to find the angle between the direction of emission and the line-of-sight at a given rotational phase ϕ_{rot} , which, in this case, is equivalent to obtaining the angle between the local magnetic field vector at point 'P' and the line-of-sight.

If the emission happens at harmonic s of the local electron gyrofrequency, the magnetic field modulus at point P is $B_1 \approx \nu/(2.8s)$, where ν is in MHz and B_1 is in gauss. The θ co-ordinate of point P

²<https://science.nrao.edu/facilities/vla/observing/callist>

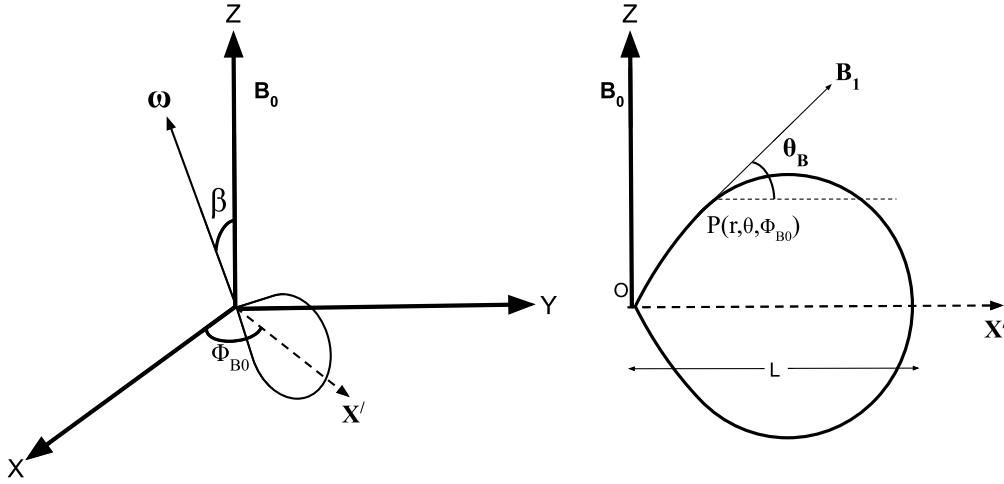


Figure D1. *Left:* The co-ordinate system used for calculating light curves due to ECME produced along certain ‘active magnetic longitudes’ (Section 4.2). The plane passing through the dipole axis and the rotation axis is defined as the XZ plane with the Z-axis along the dipole axis. This plane is rotating in the observer’s frame of reference. *Right:* the point ‘P’ on the active longitude where the ECME is produced.

can then be obtained using the following equation:

$$B_1 = \frac{B_p}{2(L \sin^2 \theta)^3} \sqrt{4 - 3 \sin^2 \theta} \quad (\text{D2})$$

where B_p is the polar field strength. The r co-ordinate can then be obtained using equation (D1). With this information, the vector magnetic field at point P (\mathbf{B}_1) can be found, which in turn will allow us to calculate the angle β_1 between the rotation axis and the magnetic field vector at point P

$$\beta_1 = \cos^{-1}(\sin \beta \cos \theta_B \cos \phi_{B0} + \cos \beta \sin \theta_B) \quad (\text{D3})$$

where β , called the obliquity, is the angle between the stellar rotational and magnetic dipole axes, and $90^\circ - \theta_B$ is the angle between the dipole axis and \mathbf{B}_1 (see right of Fig. D1). The angle between \mathbf{B}_1 and the line-of-sight, at a given rotational phase ϕ_{rot} is given by (e.g. equation 7 of Das, Mondal & Chandra 2020):

$$\cos \theta_{B1} = \cos \beta_1 \cos i_{\text{rot}} + \sin \beta_1 \sin i_{\text{rot}} \cos 2\pi(\phi_{\text{rot}} + \phi_{\text{rot}1}), \quad (\text{D4})$$

The zero point of the rotational cycle corresponds to the stellar orientation when the North magnetic pole comes closest to the line-of-sight; $\phi_{\text{rot}1}$ is the difference between the rotational longitudes corresponding to the magnetic dipole axis (\mathbf{B}_0) and the magnetic field vector \mathbf{B}_1 , and is given by the following equation (Fig. D2)

$$\cos 2\pi \phi_{\text{rot}1} = \frac{\sin \theta_B - \cos \beta \cos \beta_1}{\sin \beta \sin \beta_1}. \quad (\text{D5})$$

The observer will see the emission whenever $\theta_{B1} \approx 90^\circ$.

Following Das et al. (2020), we calculate the flux density S as a function of rotational phase ϕ_{rot} using the following equation

$$S(\phi_{\text{rot}}) = \exp\{-(\theta_{B1} - 90^\circ)^2 / 2\sigma^2\}, \quad (\text{D6})$$

where σ represents the width of the emission beam (taken to be 1° here).

To obtain the ECME light curves from the primary star, we vary the longitude (ϕ_{B0}) of the ‘active’ magnetic field line between 0° and 180° (180° – 360° is symmetric to this range). We set $B_p = 790$ G, $i_{\text{rot}} = 20^\circ$ (Shultz et al. 2015; Pablo et al. 2019, the value of B_p is a lower limit). For the obliquity β , only an upper limit is available ($\beta < 31^\circ$; Shultz et al. 2019). We set $\beta = 10^\circ$.

Under the scenario that a given magnetic field line is ‘activated’ due to the perturbation from the companion star, the value of L is likely to be a function of the separation between the two stars. If $L \sim d/2$, where d is the separation between the two stars, L varies between 2 and $4 R_*$ (using the estimates for the stellar radius, and the major axis and eccentricity of the orbit from Pablo et al. 2019).

Fig. D3 shows the light curves due to ECME produced at the northern magnetic hemisphere of the primary star for $L = 2, 3, 4 R_*$. The different colours represent magnetic field lines with different magnetic longitudes. As can be seen, a larger value of L will favour a lower observable frequency of ECME, and vice-versa.

We now consider the observed properties of the radio emission from the system. From Fig. D3, it can be seen that the ECME at the two frequencies are not necessarily observable at the same rotational phase. Besides, even for the cases where ECME at both frequencies are observable at the same rotational phase, the magnetic field lines involved are not necessarily the same. Thus, the non-observation of ECME at 750 MHz could either be due to not being able to observe the star at the right rotational phase, or that the magnetic field lines that are required to produce ECME at 750 MHz, are not ‘activated’ (the ones that come in contact with the secondary’s magnetosphere).

In the above calculation, the only parameter that is a function of the orbital phase is L . We find that the light curves are significantly affected by changes in L (e.g. for $L = 4$, ECME at 1250 MHz should not be visible at all), which can explain not being able to observe ECME at all orbital phases. Thus ECME is observable only for certain combinations of $(L, \phi_{\text{rot}}, \phi_{B0})$. The current data suggest that the enhancements are always observable at fixed orbital phases. Since the visibility of the pulses is also dependent on the rotational phase, the ECME scenario will be relevant only if the rotational frequencies are harmonics of the orbital frequency.

Since we always observed enhancements at 1250 MHz, it suggests that the ‘activated’ magnetic field lines have lower values of L . Nevertheless, in the future, it will be important to obtain observations covering the complete orbital cycle of the system so as to investigate if there is any place along the orbit where enhancements at other frequencies are observable.

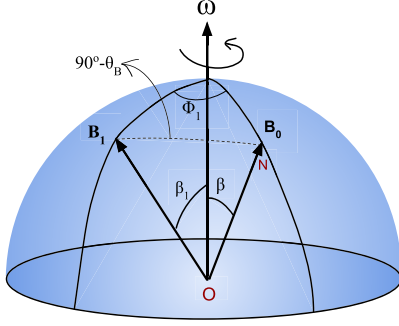


Figure D2. The difference between the rotational longitudes corresponding to the magnetic dipole axis and the magnetic field vector \mathbf{B}_1 . Here, $\phi_1 = 2\pi\phi_{\text{rot}1}$. See 4.2 for details.

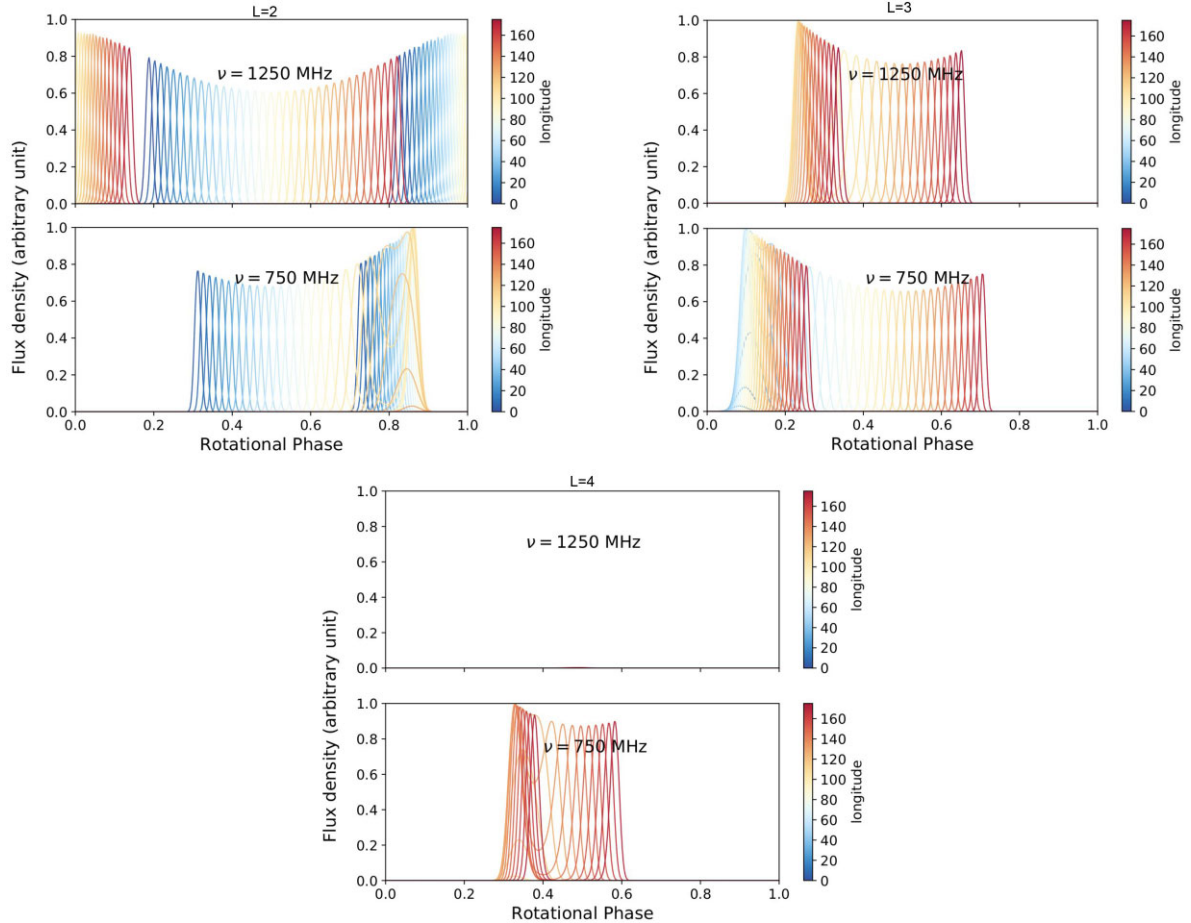


Figure D3. The simulated light curves at 1250 and 750 MHz due to ECME produced at the northern magnetic hemisphere of the primary star of the ϵ Lupi system, along magnetic field lines with longitudes lying in the range 0° – 180° . We have assumed that the dipole strength is 790 G, and the ECME is emitted at the second harmonic $s = 2$ of the local electron gyrofrequency, at right angle to the local magnetic field vector. The three figures correspond to three different values of the quantity L (see equation D1) in units of the stellar radius. Note that, the flux densities are in arbitrary units and normalized by the maximum of the combined set of light curves at the two frequencies.

This paper has been typeset from a $\text{\TeX}/\text{\LaTeX}$ file prepared by the author.